Impact of dust and temperature on primary productivity in Late Miocene oceans

Pillot Q.[1], **Sarr A-C.**[2], **Donnadieu Y.**[1], **Gramoullé A.**[1]**and Suchéras-Marx B.**[1]

[1]CEREGE, Aix Marseille Univ, CNRS, IRD, INRAE, France.
[2]Univ. Grenoble Alpes, Univ. Savoie Mont Blanc, CNRS, IRD, Univ. Gustave Eiffel, ISTerre, 38000 Grenoble, France

Key Points:

- Increased dust deposition increases primary productivity in the Miocene oceans.
- Cooling, linked to the decrease in atmospheric pCO_2 concentration, leads to a reduction in primary productivity in the Miocene oceans.
- Global aridification could have contributed to the onset of the Late Miocene Biogenic Bloom while cooling might have triggered it's decline.

Corresponding author: Pillot Q., `pillot@cerege.fr`

Abstract

Most of the primary productivity in the ocean comes from phytoplankton, and is impacted, among other things, by the amount of nutrients available, as well as by temperature. The Late Miocene and Pliocene were marked by global aridification, linked to the emergence of the large deserts, likely increasing the input of dust and thus nutrients into the ocean. There was also a global decrease in temperature during this period, linked to a decline in atmospheric CO_2 concentration. The objective of this study is to quantify the impact of dust and pCO_2 levels on primary productivity in the oceans under Late Miocene boundary conditions. New simulations were performed with the coupled ocean-atmosphere model IPSL-CM5A2 and its marine biogeochemistry component PISCES with a Late Miocene paleogeography. Our results show that an increase in dust input produces a quasi-generalized increase in primary productivity, associated with a decrease in nutrient limitation. This increase in productivity also leads to nutrient deficits in some areas. The decrease in pCO_2 levels and the associated lower water temperatures lead to a reduction in primary productivity. This decrease is mainly due to a reduction in the supply of nutrients resulting from less intense remineralization. In addition, our results show that change in carbon export resulting from change in dust input and temperature are highly heterogeneous spatially. Simulations combined with sedimentary data suggesting a link between aridification, cooling and the Biogenic Bloom of the Late Miocene and Pliocene.

1 Introduction

Phytoplanktons are responsible for most of the primary productivity in present-day oceans (Field et al., 1998). Their development depends on temperature conditions, light that limits their proliferation to surface layers and the supply of nutrients (Field et al., 1998; Balch, 2004). Among these nutrients, it is mainly the available quantity of nitrogen, iron and sometimes phosphorus that limits phytoplankton growth (C. M. Moore et al., 2013). These nutrients can come from the subsurface waters, such as in mixing zones and upwelling regions (Sarmiento et al., 2004), or from the continents via rivers (Sharples et al., 2017) and atmospheric dust (T. Jickells & Moore, 2015) transported by winds from deserts and arid source zones in particular (N. M. Mahowald et al., 2005; Hooper et al., 2019). Brief and localized episodes of dust deposition can even cause productivity blooms in some ocean areas, such as in the Yellow Sea (Shi et al., 2012), the South Atlantic (Dansie et al., 2022) and the Arabian Sea (Banerjee & Prasanna Kumar, 2014). As previously mentioned, ocean temperature is also a parameter that can influence the development of phytoplankton. This happens because temperature modulates bacteriological activity responsible for the degradation of organic matter (called remineralization or respiration), which in turn, is a source of nutrients for primary productivity (del Giorgio & Duarte, 2002). This bacteriological activity, and therefore the supply of nutrients through remineralization, increases as water temperature rises (López-Urrutia et al., 2006; Bendtsen et al., 2015). Increase in surface water temperature can on the other hand also lead to stratification of the water column, slowing down the supply of nutrients from the subsurface, balancing the remineralization effect (Behrenfeld et al., 2006).

Both the supply of dust to the ocean and temperature are parameters that have fluctuated throughout the Earth's history. During the Late Miocene ($\sim$ 11-5 Ma) and Pliocene ($\sim$ 5-3 Ma) periods, the climate became colder and drier, transitioning toward the one we know today (Steinthorsdottir et al., 2021). The significant drop in atmospheric pCO_2 at this time (from around 600 ppm in the mid-Miocene to around 400 ppm in the early Pliocene, Rae et al. (2021), Sosdian et al. (2018), de la Vega et al. (2020)) is probably responsible for this temperature decrease (Martinot et al., 2022; Hossain et al., 2023). Global cooling is associated with an increase in the latitudinal gradient of ocean surface temperature (Herbert et al., 2016; Martinot et al., 2022; Lohmann et al., 2022). The strengthening of this gradient leads to greater air mass movement in the atmosphere, causing Walker and Hadley cells

and trade winds intensification (Kamae et al., 2011). Vegetation has also changed significantly, notably with the proliferation of plants using C_4 photosynthesis (i.e. steppes) to the detriment of those using C_3 photosynthesis (i.e. forests, Cerling et al. (1997), Feakins et al. (2013), Tauxe and Feakins (2020)). This proliferation, thought to be linked to global aridification (Pound et al., 2012; Sepulchre et al., 2006), began around 10 Ma ago in tropical Africa (Polissar et al., 2019) and around 3.5 Ma ago in Australia (Andrae et al., 2018). In some places, vegetation is disappearing and replaced by major modern deserts (Schuster et al., 2006; Fujioka et al., 2009; Pound et al., 2012; Z. Zhang et al., 2014; Rech et al., 2019; Abell et al., 2020; Crocker et al., 2022). Reduced vegetation cover, due to arid climates, increases wind erosion and therefore the input of dust into the atmosphere (Hovan, 1995).

Such cooling and apparent aridification should have impacted primary productivity, though this has never been explicitely quantified. During the Late Miocene, productivity has considerably varied, with one major increase that lasted for several million years. This high productivity event, known as the Late Miocene Biogenic Bloom (LMBB), is characterized by high rates of calcite accumulation from calcareous nannofossils and planktonic foraminifera, and opals from diatoms and radiolarians (Farrell et al., 1995; Dickens & Owen, 1999; Grant & Dickens, 2002; Diester-Haass et al., 2005; Lyle & Baldauf, 2015; Drury et al., 2021; Gastaldello et al., 2023). Evidence of LMBB has been found in every oceanic basins. In the Pacific Ocean, studies suggest the presence of LMBB in the equatorial part of the basin (Farrell et al., 1995; Lyle & Baldauf, 2015; Lyle et al., 2019), in the southwestern ocean (Grant & Dickens, 2002; Gastaldello et al., 2023) and in the South China Sea (L. Zhang et al., 2009). In the Atlantic Ocean, there are traces of the event both in the northern (Diester-Haass et al., 2005), and southern basins (Hermoyian & Owen, 2001; Diester-Haass et al., 2005; Drury et al., 2021). LMBB has also been found in Indian Ocean sediments (Dickens & Owen, 1999; Hermoyian & Owen, 2001; Lübbers et al., 2019; Bolton et al., 2022). Although recorded in different oceanic basins, the LMBB appears to have a very heterogeneous spatial distribution, and many drill sites show no record of the event (Pillot et al., 2023; Lyu et al., 2023). A compilation of LMBB data has suggested a start date between 7 and 8 Ma and an end date between 2 and 3 Ma, with a maximum between 6 and 7 Ma (Pillot et al., 2023). However, studies show that the LMBB could have begun earlier, around 11-12 Ma (L. Zhang et al., 2009; Lübbers et al., 2019) and concluded earlier, around 4.5 Ma (Karatsolis et al., 2022). To explain the cause of this event, various hypotheses, which are not mutually incompatible, have been advanced in the literature. Some suggest that the increase in productivity could be the result of an increase in the supply of nutrients from the continents to the oceans (Pisias et al., 1995; Filippelli, 1997; Hermoyian & Owen, 2001; Gupta et al., 2004). This event could also result from a redistribution of nutrients in the ocean through a reorganization of ocean circulation (Dickens & Owen, 1999; Farrell et al., 1995; Pisias et al., 1995) or through a generalized increase in upwelling systems (Pillot et al., 2023). The cause of the end of the LMBB has been less discussed in the literature. Farrell et al. (1995) suggest that the definitive closure of the Central American seaway could have triggered the end of the event by preventing water exchange between the Atlantic and Pacific oceans. More recently, Karatsolis et al. (2022) propose that the hydrological cycle – and therefore the supply of nutrients via rivers – was slowed down by a decrease in insolation due to a particular orbital configuration.

Although several studies already investigated the link between pCO_2, dust and primary productivity in a present-day context (Dutkiewicz et al., 2005; Tagliabue et al., 2008, 2009; Steinacher et al., 2010), this is not the case in a geographical and climatic context corresponding to the Late Miocene, preventing the understanding of mechanisms at play in the change of primary productivity for this time period. In this study we use a coupled ocean-atmosphere model including a marine biogeochemistry component with Late Miocene boundary conditions to investigate how dust deposition and cooling affects primary production. We focus on the evolution of primary productivity in response to (1) increasing atmospheric dust deposition in the oceans and (2) decreasing CO_2 partial pressure and

associated global cooling. Our results are then discussed in the context of the LMBB (to propose a hypothesis to explain the onset and the end of this event).

2 Methods

2.1 Model

In this study, we used the IPSL-CM5A2 Earth System Model (Sepulchre et al., 2020) to perform the simulations. This model is an updated version of the IPSL-CM5A-LR model (Dufresne et al., 2013), with bias corrections and reduced computation times that enable to perform multimillennial simulations typical of paleoclimate studies. It is composed of the ocean model NEMO (Madec, 2016), the land surface and vegetation model ORCHIDEE (Krinner et al., 2005) and the atmospheric model LMDz-5A (Hourdin et al., 2013). Atmospheric and ocean component are linked by the OASIS coupler (Valcke, 2013). The atmosphere model has a resolution of 96 $\times$ 96 or 3.75° in longitude and 1.875° in latitude over 39 vertical levels. The ocean grid has 31 vertical levels (varying in thickness from 10 m near the surface to 500 m on the ocean floor) and a horizontal resolution of 2° by 2°, decreasing to 0.5° near the equator. More details on the parameterization of this model can be found in Sepulchre et al. (2020). In addition to ocean-atmosphere simulations we also use the offline version of PISCES-v2 model (Aumont et al., 2015), which is a marine biogeochemical model that simulates the main biogeochemical cycles as well as marine ecosystems (including diatoms, nanophytoplankton, microzooplankton and mesozooplankton). In this model, phytoplankton growth is limited by nutrient availability (phosphorus, nitrogen, iron and silica), light and water temperature (see Aumont et al. (2015), for detailed equations). These models have already been used to study the Miocene climate (Martinot et al., 2022; Sarr et al., 2022; Pillot et al., 2022; Burls et al., 2021; Tardif et al., 2023).

2.2 Experiments and Boundary Conditions

We used climatic fields from three Late Miocene ocean-atmosphere coupled simulations with different pCO_2 (300ppm, 420ppm and 560ppm from Sarr et al. (2022) and Martinot et al. (2022)) as inputs for the offline version of the PISCES-v2 model. The ocean dynamics for each simulation are described in the the following subsection. These simulations have been shown to mimic the amplitude of temperature decline during the Late Miocene, when compared to SST records (Martinot et al., 2022). The SSTs from the Mio420Dust and Mio560Dust simulations are in good agreement with SST recorded around the early Late Miocene (8 Ma) (Martinot et al., 2022). The SSTs from the Mio300Dust simulation are too low compared with the late Late Miocene (6 Ma) record but they could correspond to more recent times (Martinot et al., 2022). We first performed three simulations with PISCES-v2 as follow up of coupled simulations at 300 ppm, 420 ppm and 560 ppm mentioned above (Mio300Dust, Mio420Dust and Mio560Dust) that enabled us to look at the effect of temperature changes (Figure 1A) on primary productivity. In these simulations, atmospheric dust are set to pre-industrial values. The concentration of nutrients in the rivers was calibrated to the total runoff flux in order to maintain the modern total amount of nutrients transferred to the ocean. We then run three additional simulations at 420ppm : those one are forced with ocean fields identical to Mio420Dust but we varied the quantity of nutrients in atmospheric dust (iron, nitrogen and phosphorus) in order to test the effect of dust supply on primary productivity. The present-day concentration of each nutrients was divided by 2 in the Mio420Dust2 simulation, divided by 10 in the Mio420Dust10 simulation and divided by 1,000 in the Mio420NoDust simulation. The concentrations for each simulation are shown in Table 1. In order to constrain the geographical distribution of dust, satellite observations were used to constrain the geographical distribution of dust (Figure 1B, Balkanski et al. (2004)). Each nutrient has a proportion of the total concentration and an ocean solubility value. For phosphorus, the total content is 750 ppm and the solubility is 10% (N. Mahowald et al., 2008). For iron, the proportion is 3.5% (T. D. Jickells et al., 2005) with a solubility

Table 1. Experimental design. PP: Primary productivity by Phytoplanktons. EXPC: Export of carbon particles. For phosphorus, the total content is 750 ppm and the solubility is 10% (N. Mahowald et al., 2008). For iron, the proportion is 3.5% (T. D. Jickells et al., 2005) with a solubility of 20%. Finally, silica is prescribed according to J. Moore et al. (2001) with a solubility of 7.5%

Simulation	CO_2 (ppm)	Average SST (°C)	Iron from dust (Tg/yr)	Phosphorus from dust (Tg/yr)	Silice from dust (Tg/yr)	Average integrated PP ($g/m^2/day$)	Average EXPC at 100 m ($g/m^2/day$)
Mio420Dust	420	20.4	0.3312	0.03478	10.93	0.35	0.054
Mio420Dust2	420	20.4	0.1656	0.01739	5.465	0.34	0.051
Mio420Dust10	420	20.4	0.03314	0.003478	1.093	0.33	0.049
Mio420NoDust	420	20.4	0.0003539	0.00003486	0.01096	0.32	0.048
Mio300Dust	300	19.1	0.3312	0.03478	10.93	0.33	0.052
Mio560Dust	560	21.6	0.3312	0.03478	10.93	0.38	0.056

of 20%. Finally, silica is prescribed according to J. Moore et al. (2001) with a solubility of 7.5%. For phosphorus and silica, deposition is limited to the first level of the ocean model (More details can be found in Aumont et al. (2015)). Coupled simulations have been run for 3,000 years, and the last 100 years have been averaged to provide an initial state for the PISCES simulations, which have also been run for 3,000 years. Model outputs presented here are averaged over the last 100 years of each simulation.

Our simulations were carried out with a Late Miocene paleogeography based on PlioMIP geography (Haywood et al. (2020), Figure 1C). Although close to present-day geography, some differences may significantly affect the global ocean circulation and hence nutrient distribution. Those major differences include a closed Bering Seaway (Gladenkov & Gladenkov, 2004) and an Australian continent located further south than at present-day (widening the Indonesian Throughflow that connects the Indian and Pacific Oceans, Kuhnt et al. (2004)), which might be responsible for a oceanic circulation different from present-day (Brierley & Fedorov, 2016; Tan et al., 2022). The ice-sheet cover on Greenland is also smaller (Bierman et al., 2016), which also implies a different circulation compared to the modern one in the Atlantic Ocean (Davini et al., 2015; Pillot et al., 2022).

2.3 Ocean dynamics of input simulations

Ocean circulation is very similar in the Mio300Dust, Mio420Dust and Mio560Dust coupled simulations (Figure 2). The meridional overturning circulation is composed of two main cells: North Atlantic Deep Water (NADW, in blue in Figure 2A) and Antarctic Bottom Water (AABW, in red in Figure 2A). The structure of the two cells is very similar between simulations, but they are slightly weaker in the Mio560Dust simulation (Figure 2A). The formation of NADW happens during winter, and the sinking zones are located between 50° and 75° N (Figure 2B). The most important zone is located in the Labrador Sea, between 50 and 60°N, with a mixed layer depth exceeding 1,800 m depth. The location of the sinking zones are the same in all three simulations. However, in the Mio560Dust simulation, the sinking zone in the Labrador Sea is slightly larger, in detriment of the northern zones (Figure 2B). In the Southern Ocean, the sinking zone leading to AABW is located in the Weddell Sea, between 60 and 70°S, for the three simulations (Figure 2C). The depth of the mixed layer in this zone reaches 2,000 m for the Mio300Dust and Mio420Dust simulations, and exceeds 2,500 m for the Mio560Dust simulation. However, the AABW has a lower flow rate in the Mio560Dust simulation, reaching 7 Sv at the center of the cell, compared to 10 Sv for

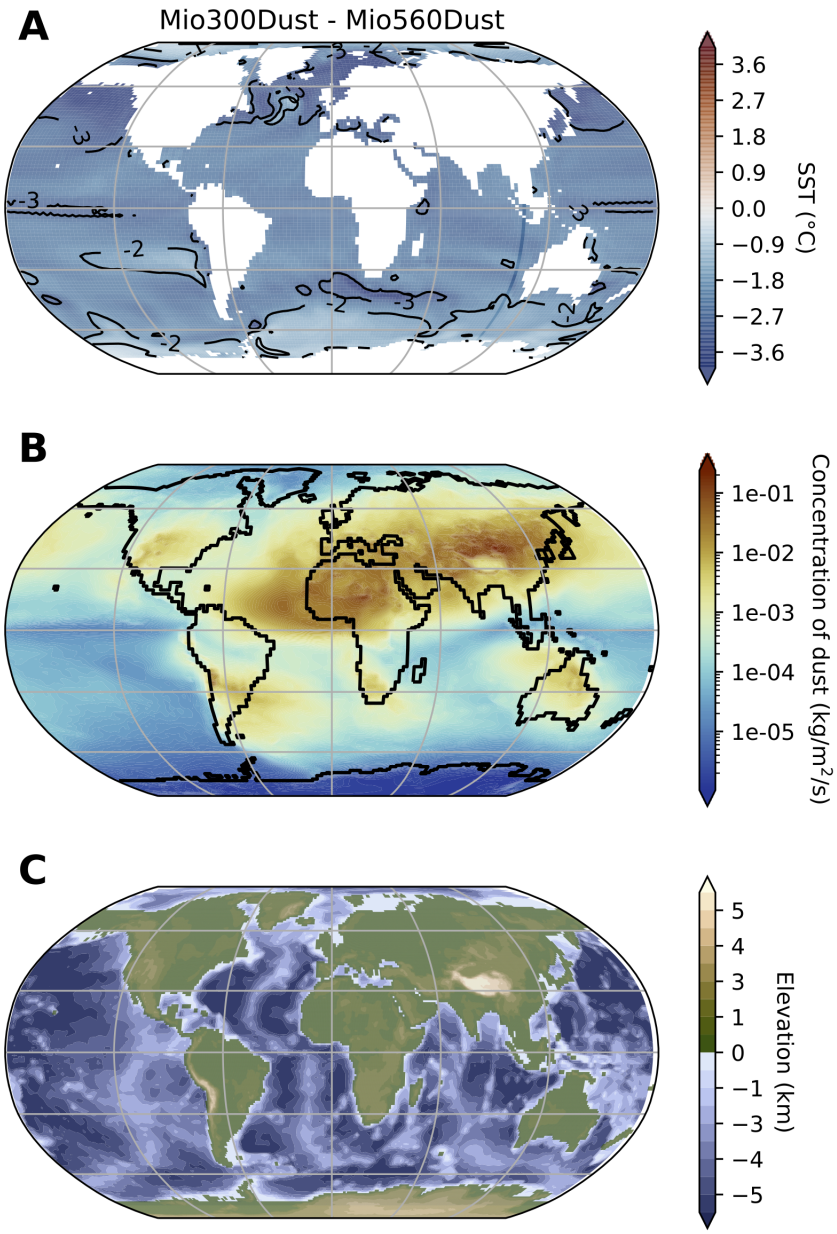

Figure 1. A: Difference in SST (°C) between the Mio300Dust and Mio560Dust simulations averaged over the year (modified from Martinot et al. (2022)). B: Atmospheric dust concentration averaged over the year (kg/m^2/s) for the Mio300Dust, Mio420Dust and Mio560Dust simulations. C: Paleogeography used for the simulations (km).

the Mio300Dust and Mio420Dust simulations (Figure 2A). At the surface, ocean circulation is organized into large gyres, just like in the modern oceans, including the North Pacific, South Pacific, North Atlantic, South Atlantic and Indian gyres (Figure 2D). The location, orientation and intensity of the gyres are identical for all three simulations. However, the circumpolar current is slightly less intense in the Mio300Dust simulation, with a mean flow of 79 Sv, compared to 92 and 90 Sv for the Mio420Dust and Mio560Dust simulations (not shown).

3 Results

3.1 Geographical distribution of productivity anomalies

3.1.1 Description of global primary productivity distribution

The spatial distribution of annual primary productivity is similar in all simulations (Figure S1). In the eastern Pacific Ocean, the high productivity is mainly located in the equatorial zone, exceeding 1 g/m^2/day in some areas (Figure 3A and 2B). This area, surrounded by two oligotrophic zones, corresponds to an important site of upwelling activity. Other productive areas are located in the western part of the basin, off the coasts of Southeast Asia and Australia. The coasts of the Indian Ocean are rich in productivity, raising the level of the entire basin, with the exception of an oligotrophic belt extending along 15°S of latitude between Madagascar and Australia (less than 0.1 g/m^2/day). In the Atlantic Ocean, waters close to the African coast have a high rate of productivity, just like waters close to Central America. Other productive areas are located in a zone between North America and Europe (at around 40°N) and between South America and Africa (at around 40°S). The Arctic and Southern Oceans exhibits low primary productivity in the simulations. In all simulations, this productivity comes mainly from nanophytoplankton, except in a few areas such as the polar oceans or some parts of the Pacific Ocean, where diatoms predominate (Figure S2, S3, S4).

3.1.2 Global distribution of dust-induced anomalies

Adding dust to the model significantly increase primary productivity in the simulations. In the Mio420NoDust simulation, the overall mean primary productivity is 0.32 g/m^2/day, compared to 0.35 g/m^2/day in the Mio420Dust simulation (Table 1). The main anomalies are located in the Atlantic and Indian Oceans, and more specifically in the waters off the coast of Africa (Figure 3C). Two areas exceed +0.2 g/m^2/day and are located off the coast of North Africa (between the Gibraltar strait and Cape Verde archipelago) and in the Arabian Sea. This is due to the spatial distribution of dust, which is highly concentrated near Africa, at the vicinity of Sahara desert. The increase in productivity in the Pacific Ocean is more heterogeneous than in other basins. In this zone, dust-derived nutrients arrive mainly via ocean currents (from other oceanic basins). The primary productivity generated by equatorial upwelling in the eastern part of the basin decreases with the increase in dust input. This behavior is also simulated along coastlines in the western and eastern part of the basins (i.e. north-western coast of North America, north-eastern coast of South America, Australian coasts, Mediterranean Sea).

3.1.3 Global distribution of pCO_2-induced anomalies

Temperature decrease triggers a global decrease in primary productivity, from 0.38 g/m^2/day on average for the Mio560Dust simulation to 0.33 g/m^2/day on average for the Mio300Dust simulation (Table 1). The signal is strongest in the Atlantic Ocean, with anomalies exceeding -0.2 g/m^2/day in some places (i.e. Gulf of Mexico, Figure 3 D). Productivity in the Indian Ocean is also declining, especially around 15°S. While there is also a significant anomaly in the north-western Pacific Ocean, other parts of the basin show a less clear signal. In the eastern Pacific Ocean, productivity increases with decreasing temperature in some

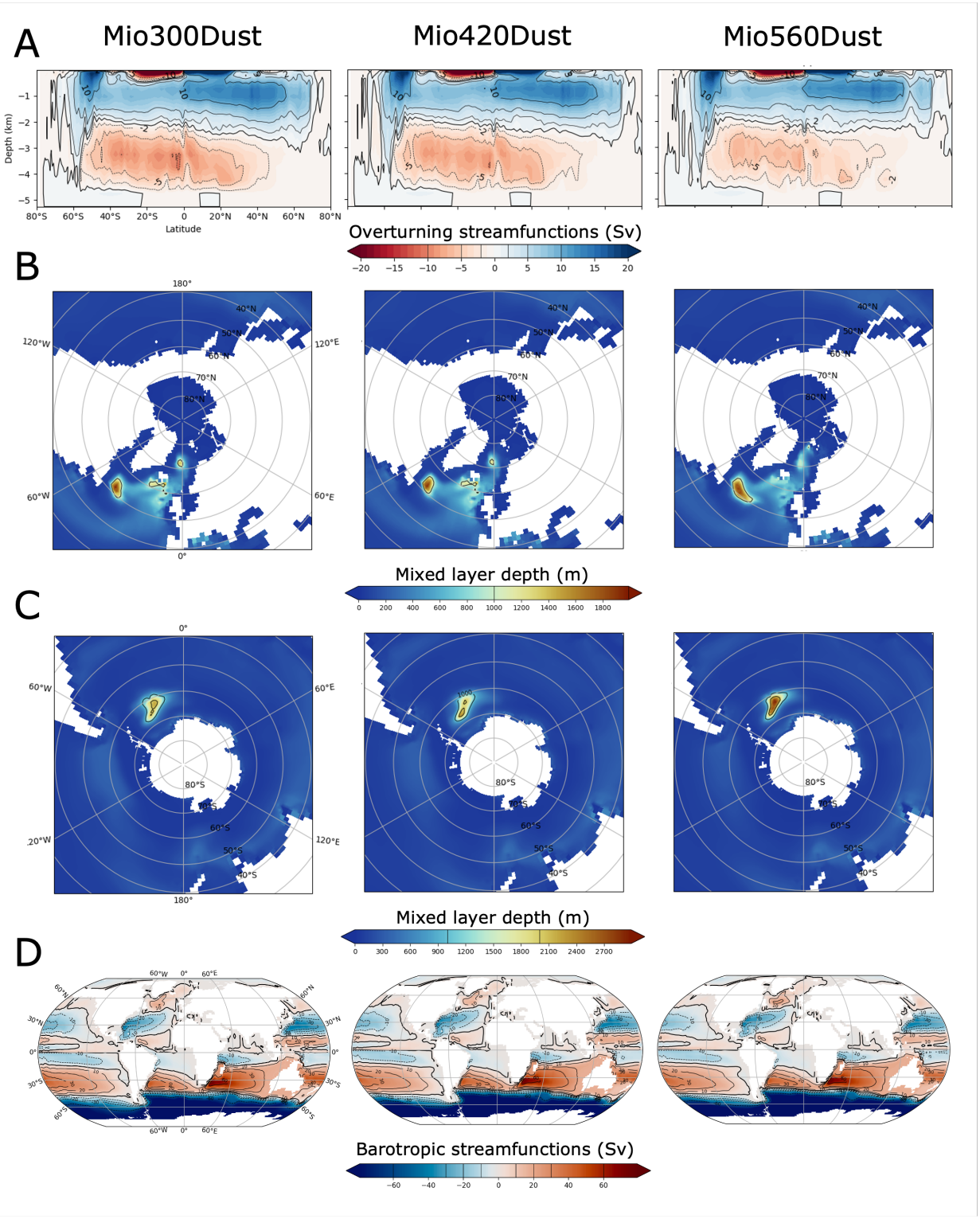

Figure 2. Left column, Mio300Dust simulation. Middle column, Mio420Dust simulation. Right column, Mio560Dust simulation. (A) Global Meridional Overturning Circulation (MOC), in Sverdup (Sv, 1 Sv = 10^6 m^3/s), computed from the global ocean. (B) Mixed layer depth (mld, meter) averaged over the winter (January-February-March). (C) Mixed layer depth (meter) averaged over the austral winter (July-August-September). (D) Mean annual barotropic stream function (Sv). In red, the water masses rotate counterclockwise and in blue, clockwise. Values represent average on the last 100 years of each simulation.

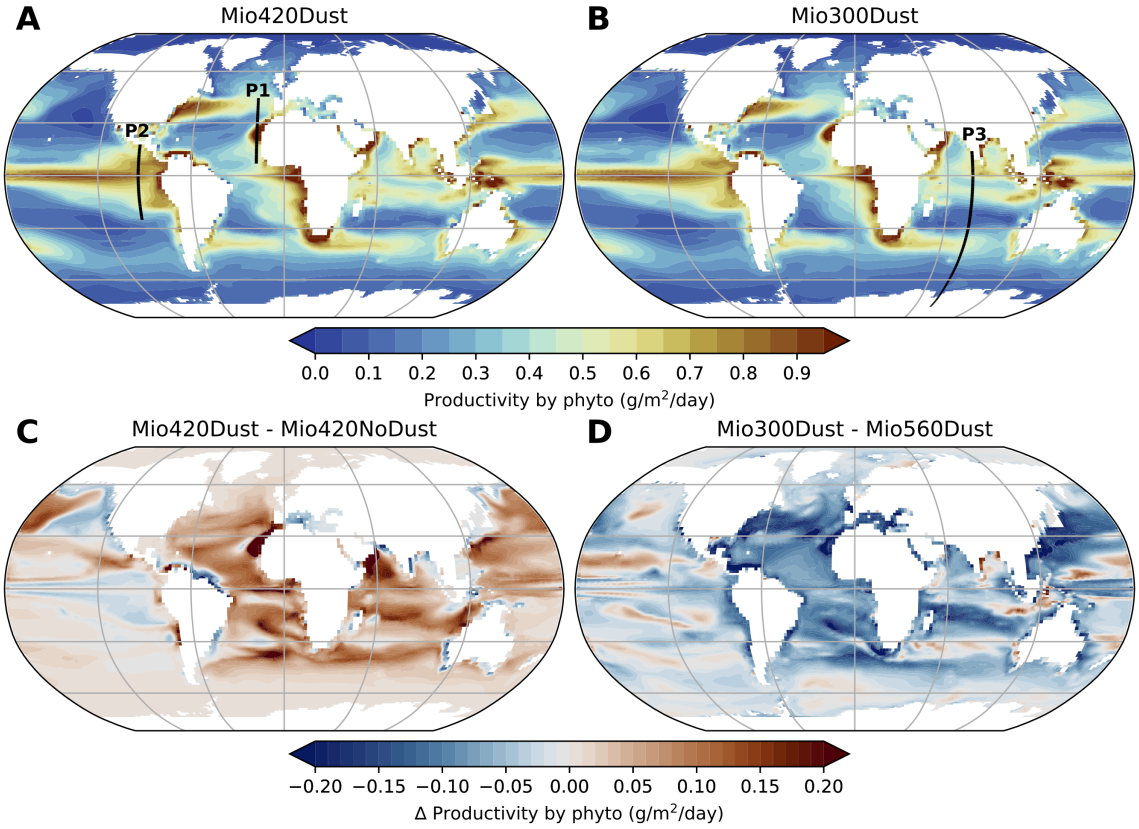

Figure 3. Ocean primary productivity by phytoplankton integrated through the water column and averaged over the year (g/m^2/day). A: Mio420Dust simulation. B: Mio300Dust simulation. C: Difference between Mio420Dust and Mio420NoDust simulations. D: Difference between Mio300Dust and Mio560Dust simulations.

areas. The spatial distribution of these zones is highly heterogeneous, with a significant positive anomaly between 0-30°N and 160°E-120°W. The coastal signal, on the other hand, is globally negative, with a decrease in productivity between Mio560Dust and Mio300Dust.

3.2 Direct impact of dust : the example of North-western African coastlines (Atlantic Ocean)

In order to emphasize mechanisms at play we decide to focus our analysis on regional scale. As mentioned previously, the area where the anomaly is most pronounced for the dust sensitivity experiments is located in the sub-tropical Atlantic Ocean, off the north-werstern African coast (around 20°W and 15-30°N, Figure 4A,B). In this area, productivity is mainly limited to the first 100 meters of the water column (below this depth, light is a limiting factor), and its vertical profile follows isodensity lines (Figure 4A) and local currentology (Figure 4D). Productivity in this zone comes mainly from nanophytoplankton (Figure 4C), whose biomass dominates that of diatoms. In this area, adding dust to the simulation (i.e. transition from Mio420NoDust to Mio420Dust) does not change the overall spatial distribution of productivity, but does increase productivity in already productive areas. The maximum increase is found between 0 and 50m depth and between 20 and 25°N, reaching +0.5 g/m^3/day with the addition of dust. The vertical profile of nutrient limitation (Fig-

ure 4E) shows that nutrients are much less limiting at this location than further north or south. The difference in nutrient limitation between the two simulations shows that at this location, nutrients are less of a limiting factor in the Mio420Dust simulation than in the Mio420NoDust simulation (Figure 4F). This very localized increase is therefore certainly due to the influx of dust from North Africa (Sahara desert) bringing nutrients to the surface ocean (Figure 1B). This correlation between productivity and dust is both geographical (as shown above) and temporal. Annual time series in this zone show that primary productivity trends are seasonal (Figure 5A). It increases in autumn, peaks in winter, then decreases during spring to reach its minimum at the end of summer. This annual cycle is flatten with decreasing dust: seasonal amplitude is more pronounced in the Mio420Dust and Mio420Dust2 simulations than in the Mio420Dust10 and Mio420NoDust simulations. This evolution of primary productivity follows very closely the evolution of the nutrient limitation term (Figure 5B). The concentration of dust in the atmosphere and its deposition in the oceans also varies according to the month of the year (Figure 5C). In the concerned area, nutrient deposition via dust increases strongly in winter/early spring and decreases in summer. Primary productivity follows the same seasonal cycle as dust deposition, highlighting a geographical and temporal correlation between the two parameters.

3.3 Remote effect of dust supply : the example of the Eastern Equatorial Pacific

Some areas, such as the EEP, show a decrease in primary productivity in response to an increase in dust supply. EEP shows a decrease in productivity between 10°N and 20°S between our Mio420NoDust and Mio420Dust simulations, with the exception of a thin band around the equator. The profile on Figure 6A shows that primary productivity in the EEP remains localized above 100m depth. At the surface, primary productivity comes mainly from nanophytoplantons, but the proportion of diatoms increases with depth in the water column (Figure 6C). The productivity anomaly between Mio420Dust and Mio420NoDust shows that positive anomaly zones (i.e., an increase in productivity following an increase in dust) are located around 25°S, 0° and 15°N (Figure 6B). Negative anomalies are located between 0° and 20°S and between 0° and 10°N, and remain below the 1024 kg/m^3 isodensity line. This pattern of positive and negative productivity anomalies follows the nutrient limitation anomalies and location of major downwelling and upwelling (Figure 6F). In this region, the downwelling cells are indeed localized respectively at 25°S and at 15°N while a main upwelling brings the waters upwards near the equator (Figure 6D). As seen previously, nutrients enter this basin mainly via oceanic circulation, rather than via direct input from dust by atmospheric circulation. A primary productivity increase that would use available nutrients at one place, would subsequently lead to a decrease in nutrients supply to other regions. This is what happens in the EEP: additional nutrient supply, due to global increase in dust input to the ocean, lead to increase productivity in downwelling and upwelling zones (25°S, 0° and 15°N), which result in water transported to adjacent region via lateral Ekman transport to be nutrient-depleted, reducing nutrient content of those waters (between 0° and 20°S and between 0° and 10°N). This is why, in the Mio420NoDust simulation, the latitudinal distribution is more homogeneous, as there are less zones of productivity (consuming nutrients) and therefore more nutrients between these zones.

3.4 Impact of temperature: Focus on the Indian Ocean

In order to highlight the mechanisms linking temperature and productivity, we decided to focus on the Indian Ocean, where the spatial distribution of the anomaly for the pCO_2 sensitivity experiments is particularly heterogeneous (Figure 3D). In this oceanic basin, decreasing atmospheric pCO_2 mostly leads to a drop in primary productivity. We decide, for further analysis, to focus on a profile along 77° E, along which the productivity response varies. In the Mio300Dust simulation, between India and Antarctica, the vertical profile of productivity shows two areas of high production: one south of India (between 10°N and

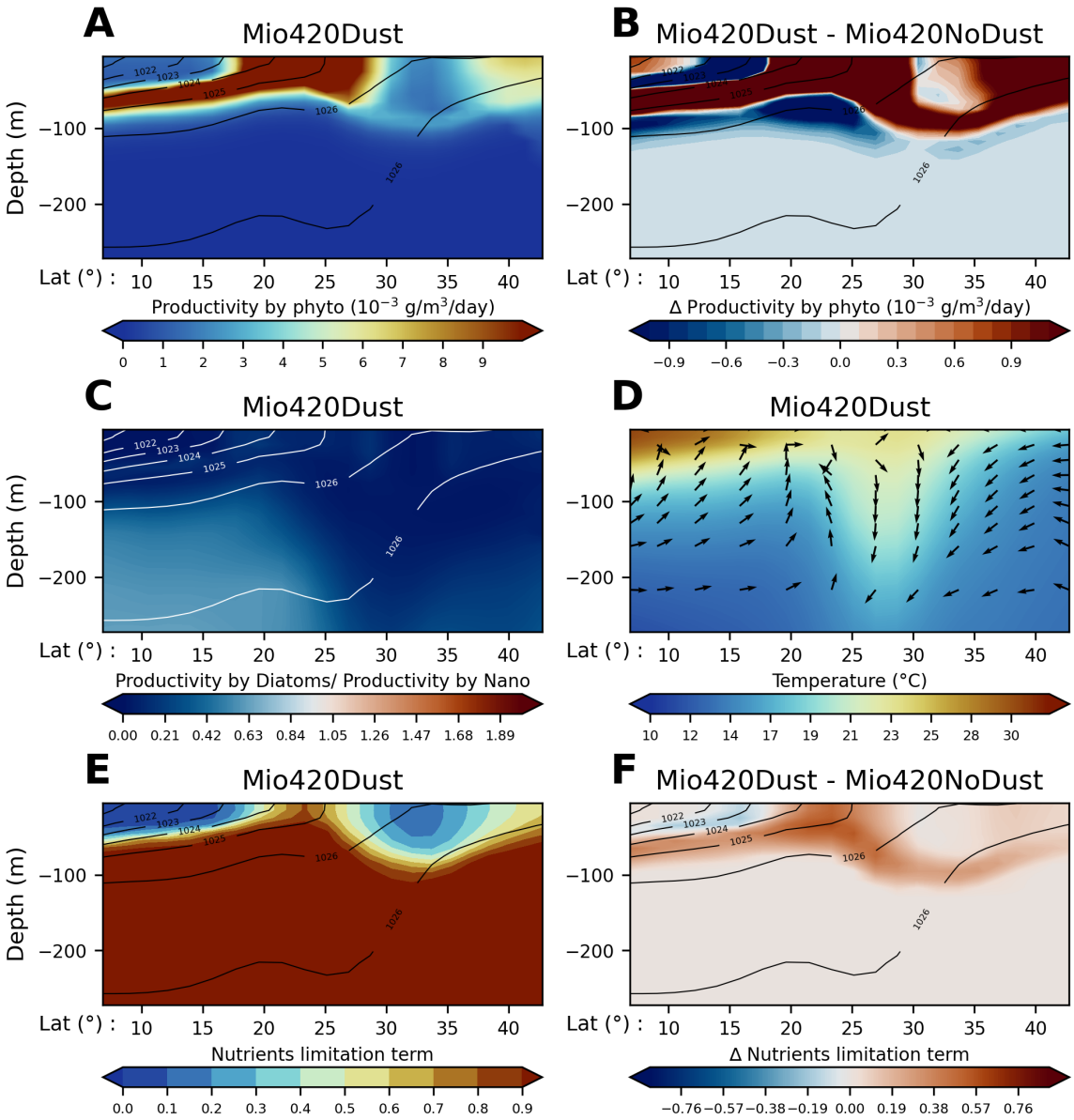

Figure 4. P1 profile, along north-western African coastlines (17°W and 5-42°N, Figure 3A), as a function of latitude (horizontal axis) and depth in meters (verticalaxis). A: Phytoplankton Primary productivity averaged over the year (g/m^2/day) with isodensity lines in black (kg/m^3) for the Mio420Dust simulation. B: Difference in phytoplankton primary productivity averaged over the year (g/m^2/day) between the Mio420Dust and Mio420NoDust simulations (with isodensity lines in black in kg/m^3 for Mio420Dust). C: Ratio between primary productivity produced by diatoms and primary productivity produced by nanophytoplankton for the Mio420Dust simulation (if >1, diatom dominance, if <1, nanophytoplankton dominance) with isodensity lines in white in kg/m^3 (for Mio420Dust). D: Water temperature (°C) with arrows representing normalized Eulerian mass transport for the Mio420Dust simulation. E: Nutrient limitation term for nanophytoplankton (between 0 and 1) for the Mio420Dust simulation. The closer the term is to 0, the more nutrients limit nanophytoplankton development (with black isodensity lines in kg/m^3 for Mio420Dust). F: Differences in nutrient-limiting term for nanophytoplankton between the Mio420Dust simulation and the Mio420NoDust simulation (with black isodensity lines in kg/m^3 for Mio420Dust).

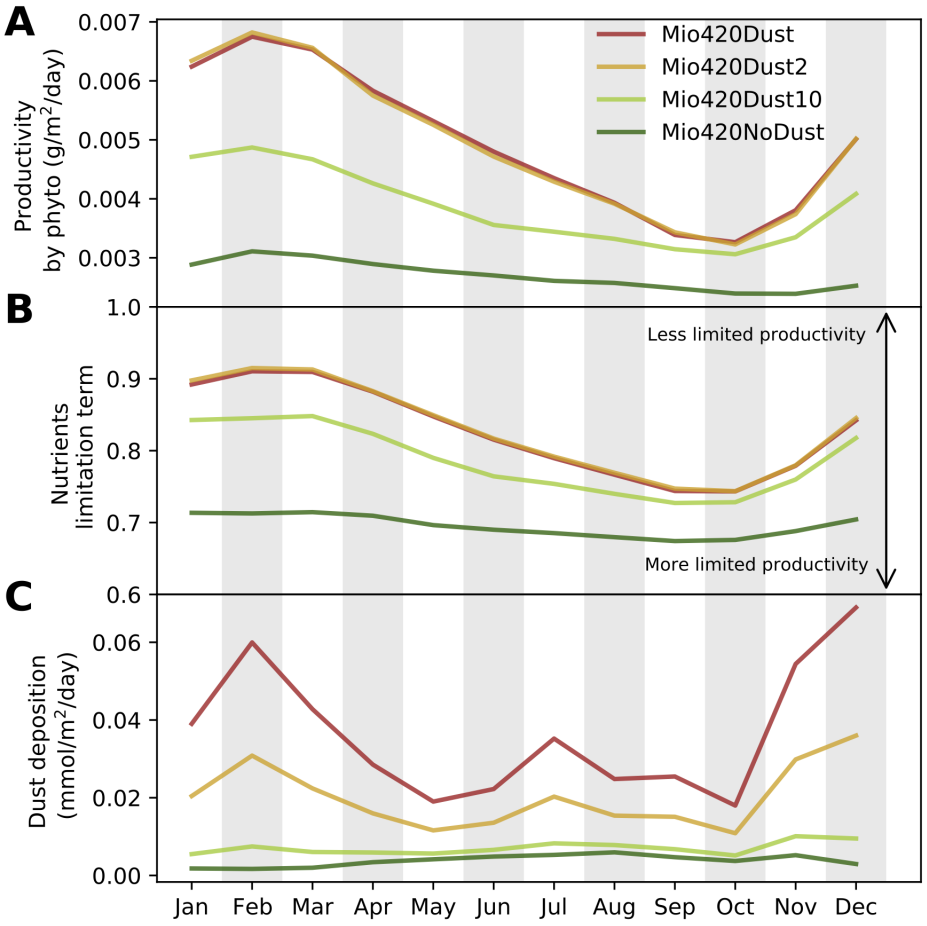

Figure 5. Annual variation of (A) Primary productivity by phytoplankton (g/m^2/day) ; (B) Nutrient limitation term (The closer the term is to 0, the more nutrients limit nanophytoplankton development) and (C) Dust deposition (Silica + Nitrogen + Phosphorus + Iron) (mmol/m^2/day) for Mio420Dust, Mio420Dust2, Mio420Dust10 and Mio420NoDust simulations. Values are averaged over an area corresponding to profile P1, along north-western African coastlines (17°W and 5-42°N, Figure 3A).

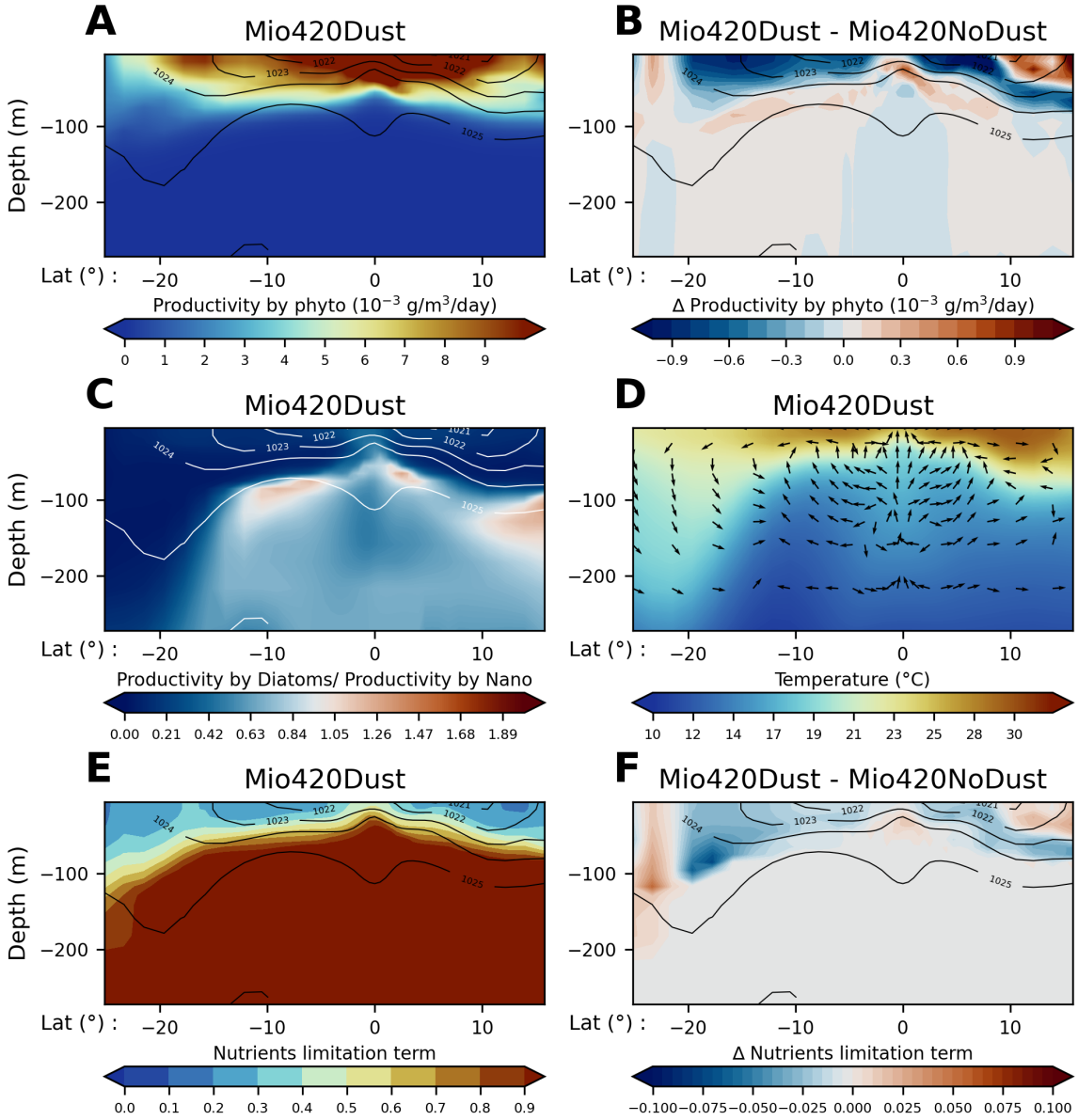

Figure 6. P2 profile, in the EEP (93°W and 25°S-15°N Figure 3A), as a function of latitude (x-axis) and depth in meters (y-axis). A: Primary phytoplankton productivity averaged over the year (g/m^2/day) with isodensity lines in black (kg/m^3) for the Mio420Dust simulation. B: Difference in phytoplankton primary productivity averaged over the year (g/m^2/day) between the Mio420Dust and Mio420NoDust simulations (with isodensity lines in black in kg/m^3 for Mio420Dust). C: Ratio between primary productivity produced by diatoms and primary productivity produced by nanophytoplankton for the Mio420Dust simulation (if >1, diatom dominance, if <1, nanophytoplankton dominance) with isodensity lines in white in kg/m^3 (for Mio420Dust). D: Water temperature (°C) for the Mio420Dust simulation with arrows representing normalized Eulerian mass transport for the Mio420Dust simulation. E: Nutrient limitation term for nanophytoplankton (between 0 and 1) for the Mio420Dust simulation. The closer the term is to 0, the more nutrients limit nanophytoplankton development (with black isodensity lines in kg/m^3 for Mio420Dust). F: Differences in nutrient-limiting term for nanophytoplankton between the Mio420Dust simulation and the Mio420NoDust simulation (with black isodensity lines in kg/m^3 for Mio420Dust).

10°S) with a maximum depth of 100m, and another further south (at around 40°S) with a maximum depth of 200m (Figure 7A). These two areas are split by a low productivity area (between 20° and 30°S) corresponding to the oligotrophic gyre of the South Indian Ocean (Figure 3B and Figure 7C). There is, however, a productivity belt at around 120m depth, following the isodensity lines. The vertical profile of productivity difference between the Mio300Dust and Mio560Dust simulations shows a very heterogeneous signal (Figure 7B), but with a majority of areas where productivity decreases as temperature decreases. Surface temperatures are on average -2.5°C colder in Mio300Dust (Figure 1C) and this anomaly extend deeper (Figure 7D). Ammonium (NH_4^+) is a nitrogen form released during remineralization and used as nutrient for primary productivity. The vertical profile of ammonium concentration follows a distribution similar to productivity in the Mio300Dust simulation (Figure 7E) and there is a decrease in ammonium concentration in the Mio300Dust compared to the Mio560Dust simulation (Figure 7F). This decrease in ammonium concentration is caused by a decrease in remineralization, which follows the temperature drop (Figure 7D). Over the whole simulation, at global scale, productivity decreases on average by 13% between Mio560Dust and Mio300Dust (Table 1), while carbon export at 100m depth only decreases by 7%. This difference in anomaly is due to remineralization, which recycles part of the productivity before it is exported downwards.

4 Discussion

4.1 Comparison of results with other modelling studies

Previous studies using marine biogeochemistry modelling have investigated the impact of dust on primary productivity in the context of future climatic projections (Dutkiewicz et al., 2005; Tagliabue et al., 2008, 2009) or for the Last Glacial Maximum (Bopp et al., 2003; Lambert et al., 2015). Tagliabue et al. (2008) also used the PISCES model to run transient simulations focusing on the impact of dust input reduction on future oceans. In their simulations, a 60% reduction in dust input leads to a 3% drop in primary productivity in the oceans. In our case, a 50% decrease in dust (from Mio420Dust to Mio420Dust2, Table 1) results in a 2.9% decrease in primary productivity, which is consistent with their results. However, the geographical distribution of productivity anomalies is different between the two studies (as in the Southern Ocean), certainly due to the difference in ocean circulation patterns between the Miocene and the present-day. Dutkiewicz et al. (2005) simulated a decrease in productivity of less than 10% in response to a 10-fold drop in dust levels, using an ocean circulation model coupled with a biogeochemical model. In comparison, productivity fell by 6% between the Mio420Dust and Mio420Dust10 simulations (Table 1). The negative correlation we simulate for the EEP in the Mio420Dust and Mio420NoDust simulation is featured as well in previous study from the literature but in the Atlantic basin. This negative correlation can be explained by oceanic circulation and has already been mentioned by Bopp et al. (2003) and Tagliabue et al. (2008). The phenomenon of increased primary productivity using the nutrients available in one place, resulting in a reduced supply of nutrients in other areas, was mentioned in Aumont et al. (2003). This same process may explain the negative coastal productivity anomalies between Mio420Dust and Mio420NoDust simulation at the continental margins of Asia and South America (for example through coastal upwelling systems).

Previous studies also look at the effect of pCO_2 change on primary productivity focusing mainly on future climate warming and its impact on primary productivity. In a model intercomparison study, (Steinacher et al., 2010) highlight a global decline in primary productivity (varying between 2% and 20% depending on the model) by 2100 in response to anthropogenic global warming. Authors attribute this decrease to warming-induced changes in ocean circulation: a slower ocean circulation, a reduced depth of the mixing layer and an increased stratification lead in the simulations to a decrease in the supply of nutrients to surface waters (with the exception of the Southern Ocean). A similar overall decrease in productivity in response to increasing temperature are found in other modeling studies (Cabré

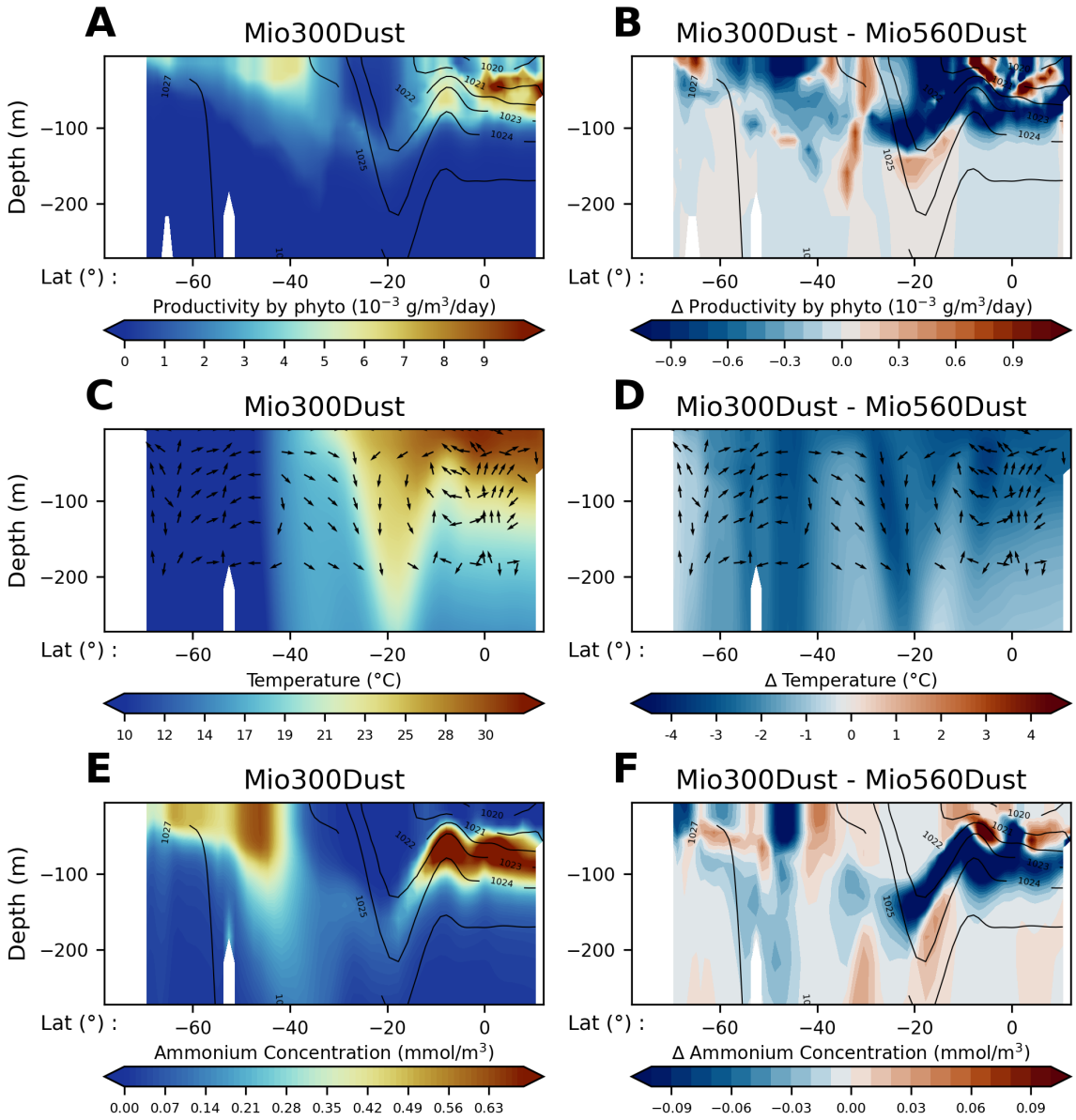

Figure 7. P3 profile, between India and Antarctica (77°E and 80°S-10°N, Figure 3B) as a function of latitude (x-axis) and depth in meters (y-axis). A: Phytoplankton primary productivity averaged over the year (g/m^2/day) with isodensity lines in black (kg/m^3) for the Mio300Dust simulation. B: Difference in phytoplankton primary productivity averaged over the year (g/m^2/day) between the Mio300Dust and Mio560Dust simulations (with isodensity lines in black in kg/m^3 for Mio300Dust). C: Water temperature (°C) for the Mio300Dust simulation with arrows representing normalized Eulerian mass transport for the Mio300Dust simulation. D: Difference in water temperature (°C) between the Mio300Dust and Mio560Dust simulations (with arrows representing normalized Eulerian mass transport for the Mio300Dust simulation). E: Ammonium concentration (mmol/m^3) for the Mio300Dust simulation (with isodensity lines in black in kg/m^3 for Mio300Dust). F: Difference in ammonium concentration (mmol/m^3) between Mio300Dust and Mio560Dust simulations (with black isodensity lines in kg/m^3 for Mio300Dust).

et al., 2015; Sarmiento et al., 2004; Kwiatkowski et al., 2019). Laufkötter et al. (2015) analyzed the changes in primary productivity simulated by nine models in the context of anthropogenic warming to 2100 (RCP8.5, IPCC). Most of the models present (including two versions of PISCES model from Aumont and Bopp (2006)) simulate a decrease in primary productivity. They find that the decrease in productivity simulated with PISCES model is mainly due to a decrease in nutrient supply following an increase in water stratification. For the other models, the simulated decrease in productivity is rather due to a warming-induced increase in grazing pressure. From Laufkötter et al. (2015), one model (PlankTOM5.3 from Buitenhuis et al. (2013)) simulates an increase in primary productivity in response to increasing temperature. The productivity changes simulated with PlankTOM5.3 are very different from changes in export production. The authors attribute this to a very strong increase in recycling efficiency (remineralization) in this model in response to a temperature increase. The importance of temperature effect on remineralization have been highlighted in Crichton et al. (2021) who used the cGENIE.muffin model with a temperature-dependent representation of the marine carbon cycle. In our simulation (Mio300Dust vs Mio560Dust), productivity rather decreases with decreasing temperature. We observe no clear difference in stratification between Mio300Dust and Mio560Dust simulations (Figure S6), this is because our simulations have been running for 3,000 years and have therefore reached an equilibrium state, even in the deep ocean. This homogenization of the temperature anomaly over the whole water column is not necessarily present in transient simulations lasting only 100 years and with a time varying forcing, as is the case in Laufkötter et al. (2015) or in (Steinacher et al., 2010). In our simulations, temperature has a major effect through remineralization (Figure 7), although we cannot totally exclude that a slight change in ocean dynamics forced by a decrease water temperature has an impact on primary productivity. Difference between our results and those published modeling work may stem from multiple factors: 1) The initial conditions of the sensitivity test (background state is different due to different initial pCO_2 and geography). 2) The model used and its productivity scheme, as seen previously (Steinacher et al., 2010; Laufkötter et al., 2015) and the simulation length (100 years vs. 3000 years). 3) Miocene ocean circulation that is different from the present-day one (Steinthorsdottir et al., 2021), affecting nutrient distribution. Primary productivity in PISCES is highly sensitive to changes in ocean circulation induced by the opening of a seaway (Ladant et al., 2018).

4.2 Carbon export and the Late Miocene Biogenic Bloom

As we show previously, primary productivity rarely extend below 100m depth (Figure 4A, Figure 6A, Figure 7A). Particulate carbon export at 100m depth increases by an average of 12.5% in response to dust deposition (Table 1). Spatial distribution of annual particulate carbon export at 100m is similar in all simulations (Figure S5). The spatial distribution of the carbon export anomaly between Mio420NoDust and Mio420Dust (Figure 8A) matches that of primary productivity (Figure 3C) and shows a heterogeneous spatial distribution. The difference is the most pronounced in the Atlantic Ocean, reaching +0.1 g/m^2/day off the North African coast. Areas that show a decrease in productivity in response to dust addition (e.g. EEP) also show a slight decrease in carbon export. We suggest that the increase in carbon export we simulate could correspond to an event like the LMBB, as this is characterized, among other aspects, by an increase in calcite accumulation in sediments. The spatial distribution of sites where this event has been observed (Pillot et al., 2023) also shows considerable heterogeneity, with sites labelled "LMBB" (in red on Figure 8) sometimes very close to sites labelled "no LMBB" (in blue on Figure 8). Geographical superimposition shows that sites labelled "LMBB" can be found in areas where simulated carbon export is increasing (e.g. South Atlantic Ocean, Australian coasts, Indian Ocean, North Pacific), but also in areas where carbon export is decreasing (EEP, South American coasts). On the other side, sites with no evidence for LMBB ("no LMBB" label) are also sometimes located in areas where simulated carbon export is changing significantly (i.e. Atlantic Ocean). The simulations show very small changes in carbon export in the Southern

Ocean, which is in agreement with the compilation of data showing no evidence of LMBB in this part of the ocean. The spatial heterogeneity of the compilation makes site-by-site model-data correlation difficult, however the scenario of increased dust supply to explain the onset of LMBB is supported by the fact that 1) most of the sites where the LMBB was identified are located in areas of simulated carbon export increase (Figure 8B) and 2) the spatial distribution of the carbon export anomaly is heterogeneous, and this is also the case for the compilation. This result tend to support Diester-Haass et al. (2006) which show a correlation between the evolution of paleoproductivity in the Late Miocene-early Pliocene in the EEP (site ODP 846, near the equator) and the evolution of wind-driven dust in this area (site ODP 848, calculated by Hovan (1995)). Crocker et al. (2022) observed an increase in dust flux in North Atlantic sediments (ODP site 659) from 8 to 5 Ma, coinciding with the onset of the LMBB between 8 and 6.5 Ma. In the Miocene, dust might also come from an external origin, such as the break-up of an asteroid, which caused an interplanetary dust particles shower on the Earth's surface around 8 Ma (Farley et al., 2006), coinciding temporally with the onset of the LMBB. However, further flux calculation are needed to evaluate the reliability of extraterrestrial supply as oceanic fertilizer. In this scenario, the distribution of dust deposits would be more homogeneous in the oceans and not linked to present-day deserts, as is the case in our study.

Our sensitivity tests for change in $ppCO_2$ show a global mean decrease of 7% in carbon export at 100m for a pCO_2 decrease of 260ppm and a global mean SST decrease of 2.5°C (Table 1). The spatial distribution of anomalies is more heterogeneous than in the dust sensitivity test (Figure 8C), but follows also the primary productivity anomaly patterns (Figure 3D). The main areas of decreasing carbon export are located in the Atlantic Ocean, the Indian Ocean (between 10° and 30°S) and the north-western Pacific Ocean. There are also areas where carbon export increases in response to lower pCO_2, such as in the EEP, the northern Indian Ocean and around Southeast Asia. The decline in Biogenic Bloom corresponds, among other things, to a decrease in calcite accumulation in marine sediments. This could be linked, in part, to the cooling associated with global drop in the partial pressure of $ppCO_2$ in the atmosphere during the Late Miocene. This hypothesis is supported by the carbon export calculated for each "LMBB" site, which is on average lower in the Mio300Dust simulation than in Mio560Dust (Figure 8D). As in the dust supply sensitivity experiments, the heterogeneity of the signal makes the geographical correlation between modeled carbon export and LMBB distribution according to Pillot et al. (2023) complex. Sites with recorded LMBB are found where simulated carbon export decreases (e.g. Atlantic Ocean) but also increases (e.g. EEP), in response to a decrease in pCO_2. Superimposing the two effects (dust supply increase + pCO_2 decrease) shows an even more heterogeneous spatial distribution of carbon export (Figure 8E). The carbon export anomaly between Mio420NoDust and Mio300Dust shows more areas corresponding to an increase in carbon export (e.g. Atlantic Ocean, Indian Ocean, EEP, North Pacific Ocean). However, the average carbon export calculated at sites labelled "LMBB" is very close to zero (Figure 8F), showing a compensatory effect of the two sensitivity tests. In summary, we could use this simulations to propose a three-stage scenario to explain the temporal evolution of the LMBB: 1) The onset of the LMBB between 8 and 6.5 Ma explained by the increase in dust deposits in the ocean linked to global aridification. During this period, the role of dust predominated over the role of pCO_2. 2) The event's maximum at around 6.5 Ma marks a balance between the effects of dust and pCO_2. 3) The decline of the LMBB between 6.5 and 2 Ma, explained by the decrease in ocean temperature (except for a short temperature increase in high latitudes around 5Ma, Herbert et al. 2016), linked to a drop in pCO_2 levels. During this period, the role of pCO_2 could have predominated over the role of dust. However, it is important to note that there are limited constraints on the temporal evolution of these two forcings, making it difficult to determine the reasons for one dominating the other. Some possible improvements to the scenario are discussed in the next subsection.

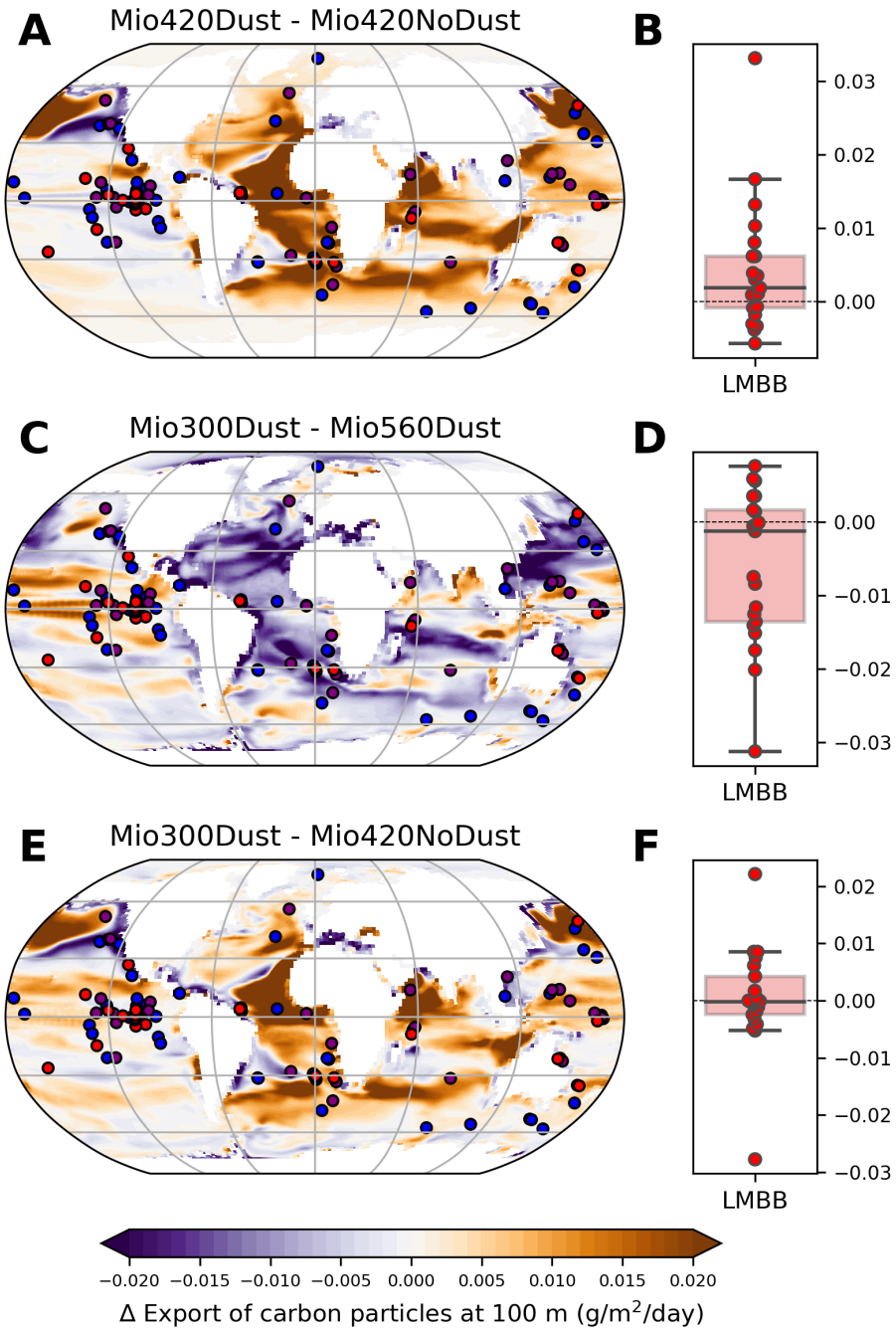

Figure 8. A), C) and E) Differences in particulate carbon export at 100m depth ($g/m^2/day$) and averaged over the year. Blue - no LMBB; purple - controversial LMBB; red - LMBB present. Dots show paleo-positions at 10 Ma of labeled sites reporting the presence or absence of LMBB, from the compilation of Pillot et al. (2023). B), D) and F) box plot showing for each site labelled "LMBB" the simulated particulate carbon export anomaly at 100m depth ($g/m^2/day$) calculated at the site paleo-location (10 Ma). A) and B) Mio420Dust - Mio420NoDust. C) and D) Mio300Dust - Mio560Dust. E) and F) Mio300Dust - Mio420NoDust.

4.3 Limitations and perspectives

Although the scenario proposed above is temporally consistent with some studies, it does not take into account several continental and oceanic parameters that evolved significantly during the Late Miocene and Pliocene, some of which have been attributed as potential causes of the LMBB. First, ocean circulation, which changed significantly during this time period, notably due to paleogeographic changes (Herold et al., 2012). Oceanic circulation in the Late Miocene and Pliocene is partly driven by North Atlantic Deep Water (NADW) formation, whose dynamics has been shown to be influenced by many geographic component that evolved during the Late Miocene to Pliocene. This make individual contributions difficult to quantify (Poore et al., 2006) and no continuous record of NADW strength exist over the entire interval. The NADW might have underwent phases of decreasing intensity, as modeled by Brierley and Fedorov (2016) in response to the sudden opening of the Bering Seaway in the early Pliocene (Gladenkov & Gladenkov, 2004; Hall et al., 2023). Phases of uplift and subsidence of the Greenland-Scotland Ridge in the Late Miocene likely caused periodic variations in NADW production (Hossain et al., 2020; Poore et al., 2006; Wright & Miller, 1996). The NADW might have been intensified by the closure of the Central American seaway (Nisancioglu et al., 2003; Schneider & Schmittner, 2006; Sepulchre et al., 2014), whose exact timing though remains debated (Molnar, 2008, 2017; Montes et al., 2015; O'Dea et al., 2016), but also by the progressive development of an ice sheet over Greenland (Pillot et al., 2022; Davini et al., 2015) for which evidences exist since 7.5 Ma (Bierman et al., 2016). In addition to NADW, phases of onset and collapse of deep-water formation in the North Pacific (NPDW) also occurred during the late Miocene and Pliocene, varying the proportion of deep water from the North Atlantic and North Pacific Oceans in the meridional overturning circulation (Abell & Winckler, 2023; Ford et al., 2022; Burls et al., 2017). Those factors impacting circulation are not all taken into account in our study as it would require additional sensitivity experiments for each to them; but they could have a drastic impact of the geographic distribution of nutrients or the intensity of upwelling, both impacting primary productivity. We though suspect that although patterns of increased/decreased productivity could be different in some other simulations, the mechanisms we evidenced should still be valid (decrease nutrient limitation with increasing dust input and decrease remineralization with decreasing temperature).

In addition to the circulation changes mentioned above and the increase in dust deposition (as investigated in this study), the evolution of nutrient supply by rivers may have also impacted primary productivity at this time. In our study we have kept the quantity of nutrients transported by rivers from the continents to the ocean constant among simulations, regardless of the dust quantity in the atmosphere or the atmospheric pCO2. The latter should affect the intensity of the runoff due to change in temperature that affect the capacity of atmosphere to hold water and therefore the hydrological cycle (Herold et al., 2011). Previous studies show evidences for change in river input of nutrient throughout the Late Miocene and Pliocene. First, some studies suggest an increase in continental weathering associated to late uplift in the Tibetan Plateau (Wang et al., 2014; Clift et al., 2020; Filippelli, 1997; Holbourn et al., 2018; Yang et al., 2019) and the uplift of the Andes at 8 Ma (Hermoyian & Owen, 2001; Curry, WB and Shackleton, NJ and Richter, C and Backman, JE and Bassinot, F and Bickert, T and Chaisson, WP and Cullen, JL and deMenocal, P and Dobson, DM and others, 1995). Secondly, river nutrient supply might have been affected by the increased input of siliceous phytoliths into the ocean due to the global spread of C4 plants (Pound et al., 2012). Moreover, the LMBB is also characterized by an increase in the export of biogenic silica (opal) in several sites of the Pacific Ocean (Cortese et al., 2004). Thirdly, in our simulation we kept orbital parameters in present day configuration but this parameter (which has a higher temporal resolution than the factors mentioned previously) can affect the intensity of the hydrological cycle (Tardif et al., 2021). A particular orbital configuration can lead to a change in insolation intensity impacting continental weathering (Karatsolis et al., 2022). Orbital parameters can also have a direct impact on dust deposition (Crocker et al., 2022) and the distribution of primary productivity (Le Mézo et al., 2017;

Beaufort et al., 2022). The evolution of nutrient supply by rivers may have contributed significantly to the evolution of global primary productivity in the Late Miocene and Pliocene. In order to clearly identify the roles of all these parameters on the onset and ending of the LMBB, further studies should focus on the impact of different mode of ocean circulation and change in runoff on primary productivity in the Late Miocene-Pliocene oceans. We also need more data with land-ocean continuum records of productivity, dust and detrital material covering the late Miocene and Pliocene.

5 Conclusion

Our simulations suggest that the evolution of marine primary productivity at the end of the Miocene could have been impacted by aridification and global cooling at this period. We show that the addition of dust in the atmosphere results in an almost generalized increase in primary productivity (due to an increase in nutrients availability) in the ocean, but with a rather heterogeneous spatial distribution. Major productivity increases are located in areas bordering major deserts, such as in the tropical Atlantic ocean. Some areas, such as the EEP, show a decrease in primary productivity in response to an increase in dust that we relate to the supply of non-consumed nutrients. On the other hand, decreasing pCO_2 in the simulations leads to an overall decrease in primary productivity in the ocean, with again an heterogeneous spatial distribution of anomalies. This is mainly due to the reduced supply of nutrients from the degradation of organic matter, which is less efficient at lower temperatures. In addition, we simulated an increase in carbon export to the ocean almost everywhere, due to the increase in dust. We suggest here that this phenomenon can be linked to the onset of LMBB, which corresponds to a calcite increase in the sediments and coincides temporally with a phase of increased dust deposition according to the literature. In a similar way, the decline in carbon export simulated in response to a decrease in atmospheric pCO_2 levels can be linked to the decline of the LMBB. The heterogeneous pattern of the spatial distribution of carbon export anomalies is consistent with the heterogeneous pattern of the LMBB data compilation from Pillot et al. (2023). In order to get a more comprehensive view of the causes of LMBB onset and decline, further simulations need to include changes in ocean circulation that occurred in the Late Miocene and Pliocene, as well as changes in nutrient inputs from rivers. But disentangling all triggering parameters might be difficult.

6 Open Research

LMDZ, XIOS, NEMO and ORCHIDEE are released under the terms of the CeCILL license. OASIS-MCT is released under the terms of the Lesser GNU General Public License (LGPL). IPSL-CM5A2 source code is publicly available through Pillot (2022) The mod.def file provides information regarding the different revisions used, namely:

- NEMOGCM branch `nemo_v3_6_STABLE` revision 6665
- XIOS2 branchs/xios-2.5 revision 1763
- IOIPSL/src svn `tags/v2_2_2`
- LMDZ5 branches/IPSLCM5A2.1 rev 3591
- branches/publications/ORCHIDEE IPSLCM5A2.1.r5307 rev 6336
- OASIS3-MCT 2.0 branch (rev 4775 IPSL server)

We recommend that you refer to the project website: `http://forge.ipsl.jussieu.fr/igcmgdoc/wiki/Doc/Config/IPSLCM5A2` for a proper installation and compilation of the environment.

All model outputs used in this study that do not come from Sarr et al. (2022) or Martinot et al. (2022) are available on the repository Pillot (2023).

Acknowledgments

We thank the CEA/ CCRT for providing access to the HPC resources of TGCC under the allocations 2021-A0110102212 and 2022-A0090102212 made by GENCI. This research was funded by the French ANR project MioCarb awarded to BSM (ANR-20-CE49-0002). A-C. Sarr is supported by a grant from Labex OSUG (Investissements d'avenir – ANR10 LABX56). The authors thank Jean-Baptiste Ladant and Marie Laugié for their help in using PISCES-v2 model. Colored maps and 2D profiles in this paper were made with perceptually uniform, color-vision-deficiency-friendly scientific color maps, developed and distributed by F. Crameri (`www.fabiocrameri.ch/colourmaps`, Crameri et al. (2020)).

References

Abell, J. T., Rahimi, S. R., Pullen, A., Lebo, Z. J., Zhang, D., Kapp, P., ... Winckler, G. (2020). A Quantitative Model-Based Assessment of Stony Desert Landscape Evolution in the Hami Basin, China: Implications for Plio-Pleistocene Dust Production in Eastern Asia. *Geophysical Research Letters*, *47*(20), e2020GL090064. Retrieved 2023-08-04, from `https://onlinelibrary.wiley.com/doi/abs/10.1029/2020GL090064` (_eprint: https://agupubs.onlinelibrary.wiley.com/doi/pdf/10.1029/2020GL090064) doi: 10.1029/2020GL090064

Abell, J. T., & Winckler, G. (2023). Long-Term Variability in Pliocene North Pacific Ocean Export Production and Its Implications for Ocean Circulation in a Warmer World. *AGU Advances*, *4*(4), e2022AV000853. Retrieved 2023-08-23, from `https://onlinelibrary.wiley.com/doi/abs/10.1029/2022AV000853` (_eprint: https://agupubs.onlinelibrary.wiley.com/doi/pdf/10.1029/2022AV000853) doi: 10.1029/2022AV000853

Andrae, J. W., McInerney, F. A., Polissar, P. J., Sniderman, J. M. K., Howard, S., Hall, P. A., & Phelps, S. R. (2018). Initial Expansion of C4 Vegetation in Australia During the Late Pliocene. *Geophysical Research Letters*, *45*(10), 4831–4840. Retrieved 2023-07-26, from `https://onlinelibrary.wiley.com/doi/abs/10.1029/2018GL077833` (_eprint: https://agupubs.onlinelibrary.wiley.com/doi/pdf/10.1029/2018GL077833) doi: 10.1029/2018GL077833

Aumont, O., & Bopp, L. (2006). Globalizing results from ocean in situ iron fertilization studies. *Global Biogeochemical Cycles*, *20*(2). Retrieved 2023-08-07, from `https://onlinelibrary.wiley.com/doi/abs/10.1029/2005GB002591` (_eprint: https://agupubs.onlinelibrary.wiley.com/doi/pdf/10.1029/2005GB002591) doi: 10.1029/2005GB002591

Aumont, O., Ethé, C., Tagliabue, A., Bopp, L., & Gehlen, M. (2015, August). PISCES-v2: an ocean biogeochemical model for carbon and ecosystem studies. *Geoscientific Model Development*, *8*(8), 2465–2513. Retrieved 2022-01-03, from `https://gmd.copernicus.org/articles/8/2465/2015/` doi: 10.5194/gmd-8-2465-2015

Aumont, O., Maier-Reimer, E., Blain, S., & Monfray, P. (2003). An ecosystem model of the global ocean including Fe, Si, P colimitations. *Global Biogeochemical Cycles*, *17*(2). Retrieved 2023-08-07, from `https://onlinelibrary.wiley.com/doi/abs/10.1029/2001GB001745` (_eprint: https://agupubs.onlinelibrary.wiley.com/doi/pdf/10.1029/2001GB001745) doi: 10.1029/2001GB001745

Balch, W. M. (2004). Re-evaluation of the physiological ecology of coccolithophores. In H. R. Thierstein & J. R. Young (Eds.), *Coccolithophores: From Molecular Processes to Global Impact* (pp. 165–190). Berlin, Heidelberg: Springer. Retrieved 2023-08-15, from `https://doi.org/10.1007/978-3-662-06278-4_7` doi: 10.1007/978-3-662-06278-4_7

Balkanski, Y., Schulz, M., Claquin, T., Moulin, C., & Ginoux, P. (2004). Global Emissions of Mineral Aerosol: Formulation and Validation using Satellite Imagery. In M. Beniston, C. Granier, P. Artaxo, & C. E. Reeves (Eds.), *Emissions of Atmospheric Trace Compounds* (Vol. 18, pp. 239–267). Dordrecht: Springer Netherlands. Retrieved

2023-08-04, from http://link.springer.com/10.1007/978-1-4020-2167-1_6 (Series Title: Advances in Global Change Research) doi: 10.1007/978-1-4020-2167-1_6

Banerjee, P., & Prasanna Kumar, S. (2014). Dust-induced episodic phytoplankton blooms in the Arabian Sea during winter monsoon. *Journal of Geophysical Research: Oceans*, *119*(10), 7123–7138. Retrieved 2023-07-31, from https://onlinelibrary.wiley.com/doi/abs/10.1002/2014JC010304 (_eprint: https://agupubs.onlinelibrary.wiley.com/doi/pdf/10.1002/2014JC010304) doi: 10.1002/2014JC010304

Beaufort, L., Bolton, C. T., Sarr, A.-C., Suchéras-Marx, B., Rosenthal, Y., Donnadieu, Y., ... Tetard, M. (2022, January). Cyclic evolution of phytoplankton forced by changes in tropical seasonality. *Nature*, *601*(7891), 79–84. Retrieved 2023-09-05, from https://www.nature.com/articles/s41586-021-04195-7 doi: 10.1038/s41586-021-04195-7

Behrenfeld, M. J., O'Malley, R. T., Siegel, D. A., McClain, C. R., Sarmiento, J. L., Feldman, G. C., ... Boss, E. S. (2006, December). Climate-driven trends in contemporary ocean productivity. *Nature*, *444*(7120), 752–755. Retrieved 2023-07-31, from https://www.nature.com/articles/nature05317 doi: 10.1038/nature05317

Bendtsen, J., Hilligsøe, K. M., Hansen, J. L., & Richardson, K. (2015, January). Analysis of remineralisation, lability, temperature sensitivity and structural composition of organic matter from the upper ocean. *Progress in Oceanography*, *130*, 125–145. Retrieved 2023-07-31, from https://linkinghub.elsevier.com/retrieve/pii/S0079661114001724 doi: 10.1016/j.pocean.2014.10.009

Bierman, P. R., Shakun, J. D., Corbett, L. B., Zimmerman, S. R., & Rood, D. H. (2016, December). A persistent and dynamic East Greenland Ice Sheet over the past 7.5 million years. *Nature*, *540*(7632), 256–260. Retrieved 2020-08-28, from http://www.nature.com/articles/nature20147 doi: 10.1038/nature20147

Bolton, C. T., Gray, E., Kuhnt, W., Holbourn, A. E., Lübbers, J., Grant, K., ... Andersen, N. (2022, April). Secular and orbital-scale variability of equatorial Indian Ocean summer monsoon winds during the late Miocene. *Climate of the Past*, *18*(4), 713–738. Retrieved 2022-08-15, from https://cp.copernicus.org/articles/18/713/2022/ doi: 10.5194/cp-18-713-2022

Bopp, L., Kohfeld, K. E., Le Quéré, C., & Aumont, O. (2003). Dust impact on marine biota and atmospheric CO2 during glacial periods. *Paleoceanography*, *18*(2). Retrieved 2023-04-25, from https://onlinelibrary.wiley.com/doi/abs/10.1029/2002PA000810 (_eprint: https://agupubs.onlinelibrary.wiley.com/doi/pdf/10.1029/2002PA000810) doi: 10.1029/2002PA000810

Brierley, C. M., & Fedorov, A. V. (2016, June). Comparing the impacts of Miocene–Pliocene changes in inter-ocean gateways on climate: Central American Seaway, Bering Strait, and Indonesia. *Earth and Planetary Science Letters*, *444*, 116–130. Retrieved 2021-05-10, from https://linkinghub.elsevier.com/retrieve/pii/S0012821X16300978 doi: 10.1016/j.epsl.2016.03.010

Buitenhuis, E. T., Hashioka, T., & Quéré, C. L. (2013). Combined constraints on global ocean primary production using observations and models. *Global Biogeochemical Cycles*, *27*(3), 847–858. Retrieved 2023-08-22, from https://onlinelibrary.wiley.com/doi/abs/10.1002/gbc.20074 (_eprint: https://agupubs.onlinelibrary.wiley.com/doi/pdf/10.1002/gbc.20074) doi: 10.1002/gbc.20074

Burls, N. J., Bradshaw, C., De Boer, A. M., Herold, N., Huber, M., Pound, M., ... Zhang, Z. (2021, January). *Simulating Miocene warmth: insights from an opportunistic Multi-Model ensemble (MioMIP1)* (preprint). Climatology (Global Change). Retrieved 2021-05-06, from http://www.essoar.org/doi/10.1002/essoar.10505870.1 doi: 10.1002/essoar.10505870.1

Burls, N. J., Fedorov, A. V., Sigman, D. M., Jaccard, S. L., Tiedemann, R., & Haug, G. H. (2017, September). Active Pacific meridional overturning circulation (PMOC) during the warm Pliocene. *Science Advances*, *3*(9), e1700156. Retrieved 2023-08-23, from https://www.science.org/doi/10.1126/sciadv.1700156 doi: 10.1126/

sciadv.1700156

Cabré, A., Marinov, I., & Leung, S. (2015, September). Consistent global responses of marine ecosystems to future climate change across the IPCC AR5 earth system models. *Climate Dynamics*, *45*(5-6), 1253–1280. Retrieved 2023-08-08, from http://link.springer.com/10.1007/s00382-014-2374-3 doi: 10.1007/s00382-014-2374-3

Cerling, T. E., Harris, J. M., MacFadden, B. J., Leakey, M. G., Quade, J., Eisenmann, V., & Ehleringer, J. R. (1997, September). Global vegetation change through the Miocene/Pliocene boundary. *Nature*, *389*(6647), 153–158. Retrieved 2022-09-22, from http://www.nature.com/articles/38229 doi: 10.1038/38229

Clift, P. D., Kulhanek, D. K., Zhou, P., Bowen, M. G., Vincent, S. M., Lyle, M., & Hahn, A. (2020, June). Chemical weathering and erosion responses to changing monsoon climate in the Late Miocene of Southwest Asia. *Geological Magazine*, *157*(6), 939–955. Retrieved 2022-07-20, from https://www.cambridge.org/core/product/identifier/S0016756819000608/type/journal_article doi: 10.1017/S0016756819000608

Cortese, G., Gersonde, R., Hillenbrand, C.-D., & Kuhn, G. (2004, August). Opal sedimentation shifts in the World Ocean over the last 15 Myr. *Earth and Planetary Science Letters*, *224*(3-4), 509–527. Retrieved 2020-11-09, from https://linkinghub.elsevier.com/retrieve/pii/S0012821X04003553 doi: 10.1016/j.epsl.2004.05.035

Crameri, F., Shephard, G. E., & Heron, P. J. (2020, December). The misuse of colour in science communication. *Nature Communications*, *11*(1), 5444. Retrieved 2022-05-26, from http://www.nature.com/articles/s41467-020-19160-7 doi: 10.1038/s41467-020-19160-7

Crichton, K. A., Wilson, J. D., Ridgwell, A., & Pearson, P. N. (2021, January). Calibration of temperature-dependent ocean microbial processes in the cGENIE.muffin (v0.9.13) Earth system model. *Geoscientific Model Development*, *14*(1), 125–149. Retrieved 2023-06-27, from https://gmd.copernicus.org/articles/14/125/2021/ (Publisher: Copernicus GmbH) doi: 10.5194/gmd-14-125-2021

Crocker, A. J., Naafs, B. D. A., Westerhold, T., James, R. H., Cooper, M. J., Röhl, U., ... Wilson, P. A. (2022, July). Astronomically controlled aridity in the Sahara since at least 11 million years ago. *Nature Geoscience*. Retrieved 2022-07-26, from https://www.nature.com/articles/s41561-022-00990-7 doi: 10.1038/s41561-022-00990-7

Curry, WB and Shackleton, NJ and Richter, C and Backman, JE and Bassinot, F and Bickert, T and Chaisson, WP and Cullen, JL and deMenocal, P and Dobson, DM and others. (1995). Leg synthesis. *Proceedings Ocean Drilling Program, Initial Reports 155*, 17–21. (Publisher: Ocean Drilling Program)

Dansie, A., Thomas, D., Wiggs, G., Baddock, M., & Ashpole, I. (2022, July). Plumes and blooms – Locally-sourced Fe-rich aeolian mineral dust drives phytoplankton growth off southwest Africa. *Science of The Total Environment*, *829*, 154562. Retrieved 2023-07-27, from https://linkinghub.elsevier.com/retrieve/pii/S0048969722016552 doi: 10.1016/j.scitotenv.2022.154562

Davini, P., von Hardenberg, J., Filippi, L., & Provenzale, A. (2015, February). Impact of Greenland orography on the Atlantic Meridional Overturning Circulation. *Geophysical Research Letters*, *42*(3), 871–879. Retrieved 2020-08-28, from http://doi.wiley.com/10.1002/2014GL062668 doi: 10.1002/2014GL062668

de la Vega, E., Chalk, T. B., Wilson, P. A., Bysani, R. P., & Foster, G. L. (2020, July). Atmospheric CO2 during the Mid-Piacenzian Warm Period and the M2 glaciation. *Scientific Reports*, *10*, 11002. Retrieved 2023-08-15, from https://www.ncbi.nlm.nih.gov/pmc/articles/PMC7347535/ doi: 10.1038/s41598-020-67154-8

del Giorgio, P. A., & Duarte, C. M. (2002, November). Respiration in the open ocean. *Nature*, *420*(6914), 379–384. Retrieved 2023-07-31, from https://www.nature.com/articles/nature01165 doi: 10.1038/nature01165

Dickens, G. R., & Owen, R. M. (1999, September). The Latest Miocene–Early Pliocene biogenic bloom: a revised Indian Ocean perspective. *Marine Geology*, *161*(1), 75–91. Retrieved 2020-11-09, from https://linkinghub.elsevier.com/retrieve/pii/S0025322799000572 doi: 10.1016/S0025-3227(99)00057-2

Diester-Haass, L., Billups, K., & Emeis, K. C. (2005). In search of the late Miocene–early Pliocene "biogenic bloom" in the Atlantic Ocean (Ocean Drilling Program Sites 982, 925, and 1088). *Paleoceanography*, *20*(4). Retrieved 2022-03-15, from http://onlinelibrary.wiley.com/doi/abs/10.1029/2005PA001139 (_eprint: https://agupubs.onlinelibrary.wiley.com/doi/pdf/10.1029/2005PA001139) doi: 10.1029/2005PA001139

Diester-Haass, L., Billups, K., & Emeis, K. C. (2006). Late Miocene carbon isotope records and marine biological productivity: Was there a (dusty) link? *Paleoceanography*, *21*(4). Retrieved 2022-03-15, from http://onlinelibrary.wiley.com/doi/abs/10.1029/2006PA001267 (_eprint: https://agupubs.onlinelibrary.wiley.com/doi/pdf/10.1029/2006PA001267) doi: 10.1029/2006PA001267

Drury, A. J., Liebrand, D., Westerhold, T., Beddow, H. M., Hodell, D. A., Rohlfs, N., ... Lourens, L. J. (2021, October). Climate, cryosphere and carbon cycle controls on Southeast Atlantic orbital-scale carbonate deposition since the Oligocene (30–0 Ma). *Climate of the Past*, *17*(5), 2091–2117. Retrieved 2022-03-03, from https://cp.copernicus.org/articles/17/2091/2021/ doi: 10.5194/cp-17-2091-2021

Dufresne, J.-L., Foujols, M.-A., Denvil, S., Caubel, A., Marti, O., Aumont, O., ... Vuichard, N. (2013, May). Climate change projections using the IPSL-CM5 Earth System Model: from CMIP3 to CMIP5. *Climate Dynamics*, *40*(9-10), 2123–2165. Retrieved 2022-01-03, from http://link.springer.com/10.1007/s00382-012-1636-1 doi: 10.1007/s00382-012-1636-1

Dutkiewicz, S., Follows, M. J., & Parekh, P. (2005). Interactions of the iron and phosphorus cycles: A three-dimensional model study. *Global Biogeochemical Cycles*, *19*(1). Retrieved 2023-08-07, from https://onlinelibrary.wiley.com/doi/abs/10.1029/2004GB002342 (_eprint: https://agupubs.onlinelibrary.wiley.com/doi/pdf/10.1029/2004GB002342) doi: 10.1029/2004GB002342

Farley, K. A., Vokrouhlický, D., Bottke, W. F., & Nesvorný, D. (2006, January). A late Miocene dust shower from the break-up of an asteroid in the main belt. *Nature*, *439*(7074), 295–297. Retrieved 2023-06-28, from https://www.nature.com/articles/nature04391 doi: 10.1038/nature04391

Farrell, J. W., Raffi, I., Janecek, T. R., Murray, D. W., Levitan, M., Dadey, K. A., ... Hovan, S. (1995). 35. LATE NEOGENE SEDIMENTATION PATTERNS IN THE EASTERN EQUATORIAL PACIFIC OCEAN. , 40.

Feakins, S. J., Levin, N. E., Liddy, H. M., Sieracki, A., Eglinton, T. I., & Bonnefille, R. (2013, March). Northeast African vegetation change over 12 m.y. *Geology*, *41*(3), 295–298. Retrieved 2023-07-26, from https://pubs.geoscienceworld.org/geology/article/41/3/295-298/131095 doi: 10.1130/G33845.1

Field, C. B., Behrenfeld, M. J., Randerson, J. T., & Falkowski, P. (1998, July). Primary Production of the Biosphere: Integrating Terrestrial and Oceanic Components. *Science*, *281*(5374), 237–240. Retrieved 2023-10-13, from https://www.science.org/doi/10.1126/science.281.5374.237 doi: 10.1126/science.281.5374.237

Filippelli, G. M. (1997). Intensification of the Asian monsoon and a chemical weathering event in the late Miocene–early Pliocene: Implications for late Neogene climate change. , 4.

Ford, H. L., Burls, N. J., Jacobs, P., Jahn, A., Caballero-Gill, R. P., Hodell, D. A., & Fedorov, A. V. (2022, August). Sustained mid-Pliocene warmth led to deep water formation in the North Pacific. *Nature Geoscience*, *15*(8), 658–663. Retrieved 2023-08-23, from https://www.nature.com/articles/s41561-022-00978-3 doi: 10.1038/s41561-022-00978-3

Fujioka, T., Chappell, J., Fifield, L. K., & Rhodes, E. J. (2009, January). Australian desert dune fields initiated with Pliocene–Pleistocene global climatic shift. *Geology*, *37*(1), 51–54. Retrieved 2023-08-18, from http://pubs.geoscienceworld.org/geology/article/37/1/51/193509/Australian-desert-dune-fields-initiated-with

doi: 10.1130/G25042A.1

Gastaldello, M. E., Agnini, C., Westerhold, T., Drury, A. J., Sutherland, R., Drake, M. K., ... Alegret, L. (2023). The Late Miocene-Early Pliocene Biogenic Bloom: An Integrated Study in the Tasman Sea. *Paleoceanography and Paleoclimatology*, *38*(4), e2022PA004565. Retrieved 2023-04-06, from https://onlinelibrary.wiley.com/doi/abs/10.1029/2022PA004565 (_eprint: https://agupubs.onlinelibrary.wiley.com/doi/pdf/10.1029/2022PA004565) doi: 10.1029/2022PA004565

Gladenkov, A. Y., & Gladenkov, Y. B. (2004). Onset of Connections between the Pacific and Arctic Oceans through the Bering Strait in the Neogene. , *12*(2), 13.

Grant, K. M., & Dickens, G. R. (2002). Coupled productivity and carbon isotope records in the southwest Paci¢c Ocean during the late Miocene^early Pliocene biogenic bloom. , 22.

Gupta, A. K., Singh, R. K., Joseph, S., & Thomas, E. (2004). Indian Ocean high-productivity event (10–8 Ma): Linked to global cooling or to the initiation of the Indian monsoons? *Geology*, *32*(9), 753. Retrieved 2020-11-09, from https://pubs.geoscienceworld.org/geology/article/32/9/753-756/103705 doi: 10.1130/G20662.1

Hall, J. R., Allison, M. S., Papadopoulos, M. T., Barfod, D. N., & Jones, S. M. (2023, April). Timing and Consequences of Bering Strait Opening: New Insights From 40Ar/39Ar Dating of the Barmur Group (Tjörnes Beds), Northern Iceland. *Paleoceanography and Paleoclimatology*, *38*(4), e2022PA004539. Retrieved 2023-09-27, from https://agupubs.onlinelibrary.wiley.com/doi/10.1029/2022PA004539 (Publisher: John Wiley & Sons, Ltd) doi: 10.1029/2022PA004539

Haywood, A. M., Tindall, J. C., Dowsett, H. J., Dolan, A. M., Foley, K. M., Hunter, S. J., ... Lunt, D. J. (2020, November). The Pliocene Model Intercomparison Project Phase 2: large-scale climate features and climate sensitivity. *Climate of the Past*, *16*(6), 2095–2123. Retrieved 2023-10-14, from https://cp.copernicus.org/articles/16/2095/2020/ (Publisher: Copernicus GmbH) doi: 10.5194/cp-16-2095-2020

Herbert, T. D., Lawrence, K. T., Tzanova, A., Peterson, L. C., Caballero-Gill, R., & Kelly, C. S. (2016, November). Late Miocene global cooling and the rise of modern ecosystems. *Nature Geoscience*, *9*(11), 843–847. Retrieved 2020-11-09, from http://www.nature.com/articles/ngeo2813 doi: 10.1038/ngeo2813

Hermoyian, C. S., & Owen, R. M. (2001). Late Miocene-early Pliocene biogenic bloom: Evidence from low-productivity regions of the Indian and Atlantic Oceans. *Paleoceanography*, *16*(1), 95–100. Retrieved 2022-03-15, from http://onlinelibrary.wiley.com/doi/abs/10.1029/2000PA000501 (_eprint: https://agupubs.onlinelibrary.wiley.com/doi/pdf/10.1029/2000PA000501) doi: 10.1029/2000PA000501

Herold, N., Huber, M., & Müller, R. D. (2011, December). Modeling the Miocene Climatic Optimum. Part I: Land and Atmosphere*. *Journal of Climate*, *24*(24), 6353–6372. Retrieved 2021-08-31, from http://journals.ametsoc.org/doi/10.1175/2011JCLI4035.1 doi: 10.1175/2011JCLI4035.1

Herold, N., Huber, M., Müller, R. D., & Seton, M. (2012, March). Modeling the Miocene climatic optimum: Ocean circulation: MODELING MIOCENE OCEAN CIRCULATION. *Paleoceanography*, *27*(1), n/a–n/a. Retrieved 2020-08-28, from http://doi.wiley.com/10.1029/2010PA002041 doi: 10.1029/2010PA002041

Holbourn, A. E., Kuhnt, W., Clemens, S. C., Kochhann, K. G. D., Jöhnck, J., Lübbers, J., & Andersen, N. (2018, December). Late Miocene climate cooling and intensification of southeast Asian winter monsoon. *Nature Communications*, *9*(1), 1584. Retrieved 2022-07-20, from http://www.nature.com/articles/s41467-018-03950-1 doi: 10.1038/s41467-018-03950-1

Hooper, J., Mayewski, P., Marx, S., Henson, S., Potocki, M., Sneed, S., ... Saunders, K. M. (2019, February). Examining links between dust deposition and phytoplankton response using ice cores. *Aeolian Research*, *36*, 45–60. Retrieved 2023-07-26, from

https://linkinghub.elsevier.com/retrieve/pii/S1875963718301101 doi: 10.1016/j.aeolia.2018.11.001

Hossain, A., Knorr, G., Jokat, W., Lohmann, G., Hochmuth, K., Gierz, P., ... Stepanek, C. (2023). The Impact of Different Atmospheric CO2 Concentrations on Large Scale Miocene Temperature Signatures. *Paleoceanography and Paleoclimatology*, *38*(2), e2022PA004438. Retrieved 2023-06-28, from https://onlinelibrary.wiley.com/doi/abs/10.1029/2022PA004438 (_eprint: https://agupubs.onlinelibrary.wiley.com/doi/pdf/10.1029/2022PA004438) doi: 10.1029/2022PA004438

Hossain, A., Knorr, G., Lohmann, G., Stärz, M., & Jokat, W. (2020, July). Simulated Thermohaline Fingerprints in Response to Different Greenland-Scotland Ridge and Fram Strait Subsidence Histories. *Paleoceanography and Paleoclimatology*, *35*(7). Retrieved 2021-05-10, from https://onlinelibrary.wiley.com/doi/abs/10.1029/2019PA003842 doi: 10.1029/2019PA003842

Hourdin, F., Foujols, M.-A., Codron, F., Guemas, V., Dufresne, J.-L., Bony, S., ... Bopp, L. (2013, May). Impact of the LMDZ atmospheric grid configuration on the climate and sensitivity of the IPSL-CM5A coupled model. *Climate Dynamics*, *40*(9-10), 2167–2192. Retrieved 2022-01-03, from http://link.springer.com/10.1007/s00382-012-1411-3 doi: 10.1007/s00382-012-1411-3

Hovan, S. A. (1995). 28. Late Cenozoic atmospheric circulation intensity and climatic history recorded by Eolian deposition in the Eastern Equatorial Pacific Ocean, Leg 138. *Proceedings of the Ocean Drilling Program, Scientific Results. Proceedings of the Ocean Drilling Program, Scientific Results*, 615–625.

Jickells, T., & Moore, C. M. (2015, December). The Importance of Atmospheric Deposition for Ocean Productivity. *Annual Review of Ecology, Evolution, and Systematics*, *46*(1), 481–501. Retrieved 2023-07-26, from https://www.annualreviews.org/doi/10.1146/annurev-ecolsys-112414-054118 doi: 10.1146/annurev-ecolsys-112414-054118

Jickells, T. D., An, Z. S., Andersen, K. K., Baker, A. R., Bergametti, G., Brooks, N., ... Torres, R. (2005, April). Global Iron Connections Between Desert Dust, Ocean Biogeochemistry, and Climate. *Science*, *308*(5718), 67–71. Retrieved 2023-07-25, from https://www.science.org/doi/10.1126/science.1105959 doi: 10.1126/science.1105959

Kamae, Y., Ueda, H., & Kitoh, A. (2011). Hadley and Walker Circulations in the Mid-Pliocene Warm Period Simulated by an Atmospheric General Circulation Model. *Journal of the Meteorological Society of Japan. Ser. II*, *89*(5), 475–493. Retrieved 2022-09-26, from http://www.jstage.jst.go.jp/article/jmsj/89/5/89_5_475/_article doi: 10.2151/jmsj.2011-505

Karatsolis, B. ., Lougheed, B. C., De Vleeschouwer, D., & Henderiks, J. (2022, December). Abrupt conclusion of the late Miocene-early Pliocene biogenic bloom at 4.6-4.4 Ma. *Nature Communications*, *13*(1), 353. Retrieved 2022-01-25, from https://www.nature.com/articles/s41467-021-27784-6 doi: 10.1038/s41467-021-27784-6

Krinner, G., Viovy, N., de Noblet-Ducoudré, N., Ogée, J., Polcher, J., Friedlingstein, P., ... Prentice, I. C. (2005, March). A dynamic global vegetation model for studies of the coupled atmosphere-biosphere system: DVGM FOR COUPLED CLIMATE STUDIES. *Global Biogeochemical Cycles*, *19*(1). Retrieved 2022-01-03, from http://doi.wiley.com/10.1029/2003GB002199 doi: 10.1029/2003GB002199

Kuhnt, W., Holbourn, A., Hall, R., Zuvela, M., & Käse, R. (2004). Neogene History of the Indonesian Throughflow. In *Continent-Ocean Interactions Within East Asian Marginal Seas* (pp. 299–320). American Geophysical Union (AGU). Retrieved 2022-09-22, from http://onlinelibrary.wiley.com/doi/abs/10.1029/149GM16 (_eprint: https://agupubs.onlinelibrary.wiley.com/doi/pdf/10.1029/149GM16) doi: 10.1029/149GM16

Kwiatkowski, L., Aumont, O., & Bopp, L. (2019). Consistent trophic amplification of marine biomass declines under climate change. *Global Change Biology*, *25*(1), 218–229.

Retrieved 2023-04-21, from https://onlinelibrary.wiley.com/doi/abs/10.1111/gcb.14468 (_eprint: https://onlinelibrary.wiley.com/doi/pdf/10.1111/gcb.14468) doi: 10.1111/gcb.14468

Ladant, J.-B., Donnadieu, Y., Bopp, L., Lear, C. H., & Wilson, P. A. (2018, March). Meridional Contrasts in Productivity Changes Driven by the Opening of Drake Passage. *Paleoceanography and Paleoclimatology*, *33*(3), 302–317. Retrieved 2020-08-28, from http://doi.wiley.com/10.1002/2017PA003211 doi: 10.1002/2017PA003211

Lambert, F., Tagliabue, A., Shaffer, G., Lamy, F., Winckler, G., Farias, L., ... De Pol-Holz, R. (2015). Dust fluxes and iron fertilization in Holocene and Last Glacial Maximum climates. *Geophysical Research Letters*, *42*(14), 6014–6023. Retrieved 2023-06-28, from https://onlinelibrary.wiley.com/doi/abs/10.1002/2015GL064250 (_eprint: https://agupubs.onlinelibrary.wiley.com/doi/pdf/10.1002/2015GL064250) doi: 10.1002/2015GL064250

Laufkötter, C., Vogt, M., Gruber, N., Aita-Noguchi, M., Aumont, O., Bopp, L., ... Völker, C. (2015, December). Drivers and uncertainties of future global marine primary production in marine ecosystem models. *Biogeosciences*, *12*(23), 6955–6984. Retrieved 2023-08-22, from https://bg.copernicus.org/articles/12/6955/2015/bg-12-6955-2015.html (Publisher: Copernicus GmbH) doi: 10.5194/bg-12-6955-2015

Le Mézo, P., Beaufort, L., Bopp, L., Braconnot, P., & Kageyama, M. (2017, July). From monsoon to marine productivity in the Arabian Sea: insights from glacial and interglacial climates. *Climate of the Past*, *13*(7), 759–778. Retrieved 2023-09-05, from https://cp.copernicus.org/articles/13/759/2017/cp-13-759-2017.html (Publisher: Copernicus GmbH) doi: 10.5194/cp-13-759-2017

Lohmann, G., Knorr, G., Hossain, A., & Stepanek, C. (2022). Effects of CO2 and Ocean Mixing on Miocene and Pliocene Temperature Gradients. *Paleoceanography and Paleoclimatology*, *37*(2), e2020PA003953. Retrieved 2023-02-14, from https://onlinelibrary.wiley.com/doi/abs/10.1029/2020PA003953 (_eprint: https://agupubs.onlinelibrary.wiley.com/doi/pdf/10.1029/2020PA003953) doi: 10.1029/2020PA003953

Lyle, M., & Baldauf, J. (2015, September). Biogenic sediment regimes in the Neogene equatorial Pacific, IODP Site U1338: Burial, production, and diatom community. *Palaeogeography, Palaeoclimatology, Palaeoecology*, *433*, 106–128. Retrieved 2020-11-09, from https://linkinghub.elsevier.com/retrieve/pii/S0031018215001868 doi: 10.1016/j.palaeo.2015.04.001

Lyle, M., Drury, A. J., Tian, J., Wilkens, R., & Westerhold, T. (2019, September). Late Miocene to Holocene high-resolution eastern equatorial Pacific carbonate records: stratigraphy linked by dissolution and paleoproductivity. *Climate of the Past*, *15*(5), 1715–1739. Retrieved 2021-01-25, from https://cp.copernicus.org/articles/15/1715/2019/ doi: 10.5194/cp-15-1715-2019

Lyu, J., Auer, G., Bialik, O. M., Christensen, B., Yamaoka, R., & De Vleeschouwer, D. (2023, December). Astronomically-Paced Changes in Paleoproductivity, Winnowing, and Mineral Flux Over Broken Ridge (Indian Ocean) Since the Early Miocene. *Paleoceanography and Paleoclimatology*, *38*(12), e2023PA004761. Retrieved 2023-12-19, from https://agupubs.onlinelibrary.wiley.com/doi/10.1029/2023PA004761 doi: 10.1029/2023PA004761

López-Urrutia, , San Martin, E., Harris, R. P., & Irigoien, X. (2006, June). Scaling the metabolic balance of the oceans. *Proceedings of the National Academy of Sciences*, *103*(23), 8739–8744. Retrieved 2023-07-31, from https://pnas.org/doi/full/10.1073/pnas.0601137103 doi: 10.1073/pnas.0601137103

Lübbers, J., Kuhnt, W., Holbourn, A., Bolton, C., Gray, E., Usui, Y., ... Andersen, N. (2019, May). The Middle to Late Miocene "Carbonate Crash" in the Equatorial Indian Ocean. *Paleoceanography and Paleoclimatology*, *34*(5), 813–832. Retrieved 2022-09-19, from https://hal.archives-ouvertes.fr/hal-02341889 (Publisher: American Geophysical Union) doi: 10.1029/2018PA003482

Madec, G. (2016). NEMO ocean engine. , 396.

Mahowald, N., Jickells, T. D., Baker, A. R., Artaxo, P., Benitez-Nelson, C. R., Bergametti, G., ... Tsukuda, S. (2008, December). Global distribution of atmospheric phosphorus sources, concentrations and deposition rates, and anthropogenic impacts: GLOBAL ATMOSPHERIC PHOSPHORUS. *Global Biogeochemical Cycles*, *22*(4), n/a–n/a. Retrieved 2023-07-25, from http://doi.wiley.com/10.1029/2008GB003240 doi: 10.1029/2008GB003240

Mahowald, N. M., Baker, A. R., Bergametti, G., Brooks, N., Duce, R. A., Jickells, T. D., ... Tegen, I. (2005). Atmospheric global dust cycle and iron inputs to the ocean. *Global Biogeochemical Cycles*, *19*(4). Retrieved 2023-07-31, from https://onlinelibrary.wiley.com/doi/abs/10.1029/2004GB002402 (_eprint: https://agupubs.onlinelibrary.wiley.com/doi/pdf/10.1029/2004GB002402) doi: 10.1029/2004GB002402

Martinot, C., Bolton, C. T., Sarr, A.-C., Donnadieu, Y., Garcia, M., Gray, E., & Tachikawa, K. (2022). Drivers of Late Miocene Tropical Sea Surface Cooling: A New Perspective From the Equatorial Indian Ocean. *Paleoceanography and Paleoclimatology*, *37*(10), e2021PA004407. Retrieved 2023-01-11, from https://onlinelibrary.wiley.com/doi/abs/10.1029/2021PA004407 (_eprint: https://agupubs.onlinelibrary.wiley.com/doi/pdf/10.1029/2021PA004407) doi: 10.1029/2021PA004407

Molnar, P. (2008). Closing of the Central American Seaway and the Ice Age: A critical review. *Paleoceanography*, *23*(2). Retrieved 2023-09-05, from https://onlinelibrary.wiley.com/doi/abs/10.1029/2007PA001574 (_eprint: https://agupubs.onlinelibrary.wiley.com/doi/pdf/10.1029/2007PA001574) doi: 10.1029/2007PA001574

Molnar, P. (2017, June). Comment (2) on "Formation of the Isthmus of Panama" by O'Dea *et al* . *Science Advances*, *3*(6), e1602320. Retrieved 2023-09-05, from https://www.science.org/doi/10.1126/sciadv.1602320 doi: 10.1126/sciadv.1602320

Montes, C., Cardona, A., Jaramillo, C., Pardo, A., Silva, J. C., Valencia, V., ... Nino, H. (2015, April). Middle Miocene closure of the Central American Seaway. *Science*, *348*(6231), 226–229. Retrieved 2021-05-10, from https://www.sciencemag.org/lookup/doi/10.1126/science.aaa2815 doi: 10.1126/science.aaa2815

Moore, C. M., Mills, M. M., Arrigo, K. R., Berman-Frank, I., Bopp, L., Boyd, P. W., ... Ulloa, O. (2013, September). Processes and patterns of oceanic nutrient limitation. *Nature Geoscience*, *6*(9), 701–710. Retrieved 2023-07-27, from https://www.nature.com/articles/ngeo1765 doi: 10.1038/ngeo1765

Moore, J., Doney, S. C., Glover, D. M., & Fung, I. Y. (2001, January). Iron cycling and nutrient-limitation patterns in surface waters of the World Ocean. *Deep Sea Research Part II: Topical Studies in Oceanography*, *49*(1-3), 463–507. Retrieved 2023-07-25, from https://linkinghub.elsevier.com/retrieve/pii/S0967064501001096 doi: 10.1016/S0967-0645(01)00109-6

Nisancioglu, K. H., Raymo, M. E., & Stone, P. H. (2003, March). Reorganization of Miocene deep water circulation in response to the shoaling of the Central American Seaway: REORGANIZATION OF MIOCENE DEEP WATER CIRCULATION. *Paleoceanography*, *18*(1), n/a–n/a. Retrieved 2021-05-10, from http://doi.wiley.com/10.1029/2002PA000767 doi: 10.1029/2002PA000767

O'Dea, A., Lessios, H. A., Coates, A. G., Eytan, R. I., Restrepo-Moreno, S. A., Cione, A. L., ... Jackson, J. B. C. (2016, August). Formation of the Isthmus of Panama. *Science Advances*, *2*(8), e1600883. Retrieved 2022-09-22, from https://www.science.org/doi/10.1126/sciadv.1600883 doi: 10.1126/sciadv.1600883

Pillot, Q. (2022). *IPSL-CM5A2 source code used for "Evolution of ocean circulation in the North Atlantic Ocean during the Miocene: impact of the Greenland Ice Sheet and the Eastern Tethys Seaway".* Zenodo. Retrieved from https://doi.org/10.5281/zenodo.6772699 ([Software]) doi: 10.5281/zenodo.6772699

Pillot, Q. (2023). *Data For "Impact of dust and temperature on primary productivity in Late Miocene oceans".* Zenodo. Retrieved from https://doi.org/10.5281/zenodo

.10407477 ([Dataset]) doi: 10.5281/zenodo.10407476

Pillot, Q., Donnadieu, Y., Sarr, A.-C., Ladant, J.-B., & Suchéras-Marx, B. (2022). Evolution of Ocean Circulation in the North Atlantic Ocean During the Miocene: Impact of the Greenland Ice Sheet and the Eastern Tethys Seaway. *Paleoceanography and Paleoclimatology*, *37*(8), e2022PA004415. Retrieved 2022-09-07, from http://onlinelibrary.wiley.com/doi/abs/10.1029/2022PA004415 (_eprint: https://agupubs.onlinelibrary.wiley.com/doi/pdf/10.1029/2022PA004415) doi: 10.1029/2022PA004415

Pillot, Q., Suchéras-Marx, B., Sarr, A.-C., Bolton, C. T., & Donnadieu, Y. (2023). A Global Reassessment of the Spatial and Temporal Expression of the Late Miocene Biogenic Bloom. *Paleoceanography and Paleoclimatology*, *38*(3), e2022PA004564. Retrieved 2023-03-30, from https://onlinelibrary.wiley.com/doi/abs/10.1029/2022PA004564 (_eprint: https://agupubs.onlinelibrary.wiley.com/doi/pdf/10.1029/2022PA004564) doi: 10.1029/2022PA004564

Pisias, N., Mayer, L., Janecek, T., Palmer-Julson, A., & van Andel, T. (Eds.). (1995). *Proceedings of the Ocean Drilling Program, 138 Scientific Results* (Vol. 138). Ocean Drilling Program. Retrieved 2020-12-15, from http://www-odp.tamu.edu/publications/138_SR/138TOC.HTM doi: 10.2973/odp.proc.sr.138.1995

Polissar, P. J., Rose, C., Uno, K. T., Phelps, S. R., & deMenocal, P. (2019, August). Synchronous rise of African C4 ecosystems 10 million years ago in the absence of aridification. *Nature Geoscience*, *12*(8), 657–660. Retrieved 2023-07-26, from https://www.nature.com/articles/s41561-019-0399-2 doi: 10.1038/s41561-019-0399-2

Poore, H. R., Samworth, R., White, N. J., Jones, S. M., & McCave, I. N. (2006, June). Neogene overflow of Northern Component Water at the Greenland-Scotland Ridge: NEOGENE OVERFLOW OF NCW. *Geochemistry, Geophysics, Geosystems*, *7*(6), n/a–n/a. Retrieved 2020-08-28, from http://doi.wiley.com/10.1029/2005GC001085 doi: 10.1029/2005GC001085

Pound, M. J., Haywood, A. M., Salzmann, U., & Riding, J. B. (2012, April). Global vegetation dynamics and latitudinal temperature gradients during the Mid to Late Miocene (15.97–5.33Ma). *Earth-Science Reviews*, *112*(1-2), 1–22. Retrieved 2022-07-04, from https://linkinghub.elsevier.com/retrieve/pii/S0012825212000165 doi: 10.1016/j.earscirev.2012.02.005

Rae, J. W., Zhang, Y. G., Liu, X., Foster, G. L., Stoll, H. M., & Whiteford, R. D. (2021, May). Atmospheric CO_2 over the Past 66 Million Years from Marine Archives. *Annual Review of Earth and Planetary Sciences*, *49*(1), 609–641. Retrieved 2021-09-01, from https://www.annualreviews.org/doi/10.1146/annurev-earth-082420-063026 doi: 10.1146/annurev-earth-082420-063026

Rech, J. A., Currie, B. S., Jordan, T. E., Riquelme, R., Lehmann, S. B., Kirk-Lawlor, N. E., ... Gooley, J. T. (2019, January). Massive middle Miocene gypsic paleosols in the Atacama Desert and the formation of the Central Andean rain-shadow. *Earth and Planetary Science Letters*, *506*, 184–194. Retrieved 2023-08-18, from https://linkinghub.elsevier.com/retrieve/pii/S0012821X18306423 doi: 10.1016/j.epsl.2018.10.040

Sarmiento, J. L., Gruber, N., Brzezinski, M. A., & Dunne, J. P. (2004, January). High-latitude controls of thermocline nutrients and low latitude biological productivity. *Nature*, *427*(6969), 56–60. Retrieved 2023-07-27, from https://www.nature.com/articles/nature02127 doi: 10.1038/nature02127

Sarr, A.-C., Donnadieu, Y., Bolton, C. T., Ladant, J.-B., Licht, A., Fluteau, F., ... Dupont-Nivet, G. (2022, April). Neogene South Asian monsoon rainfall and wind histories diverged due to topographic effects. *Nature Geoscience*, *15*(4), 314–319. Retrieved 2022-06-22, from https://www.nature.com/articles/s41561-022-00919-0 doi: 10.1038/s41561-022-00919-0

Schneider, B., & Schmittner, A. (2006, June). Simulating the impact of the Panamanian seaway closure on ocean circulation, marine productivity and nutrient cy-

cling. *Earth and Planetary Science Letters*, *246*(3-4), 367–380. Retrieved 2021-10-28, from https://linkinghub.elsevier.com/retrieve/pii/S0012821X0600330X doi: 10.1016/j.epsl.2006.04.028

Schuster, M., Duringer, P., Ghienne, J.-F., Vignaud, P., Mackaye, H. T., Likius, A., & Brunet, M. (2006, February). The Age of the Sahara Desert. *Science*, *311*(5762), 821–821. Retrieved 2022-07-19, from https://www.science.org/doi/10.1126/science.1120161 doi: 10.1126/science.1120161

Sepulchre, P., Arsouze, T., Donnadieu, Y., Dutay, J.-C., Jaramillo, C., Le Bras, J., ... Waite, A. J. (2014, March). Consequences of shoaling of the Central American Seaway determined from modeling Nd isotopes. *Paleoceanography*, *29*(3), 176–189. Retrieved 2021-05-10, from http://doi.wiley.com/10.1002/2013PA002501 doi: 10.1002/2013PA002501

Sepulchre, P., Caubel, A., Ladant, J.-B., Bopp, L., Boucher, O., Braconnot, P., ... Tardif, D. (2020, July). IPSL-CM5A2 – an Earth system model designed for multi-millennial climate simulations. *Geoscientific Model Development*, *13*(7), 3011–3053. Retrieved 2022-01-03, from https://gmd.copernicus.org/articles/13/3011/2020/ doi: 10.5194/gmd-13-3011-2020

Sepulchre, P., Ramstein, G., Fluteau, F., Schuster, M., Tiercelin, J.-J., & Brunet, M. (2006, September). Tectonic Uplift and Eastern Africa Aridification. *Science*, *313*(5792), 1419–1423. Retrieved 2023-08-04, from https://www.science.org/doi/10.1126/science.1129158 doi: 10.1126/science.1129158

Sharples, J., Middelburg, J. J., Fennel, K., & Jickells, T. D. (2017). What proportion of riverine nutrients reaches the open ocean? *Global Biogeochemical Cycles*, *31*(1), 39–58. Retrieved 2023-07-27, from https://onlinelibrary.wiley.com/doi/abs/10.1002/2016GB005483 (_eprint: https://agupubs.onlinelibrary.wiley.com/doi/pdf/10.1002/2016GB005483) doi: 10.1002/2016GB005483

Shi, J.-H., Gao, H.-W., Zhang, J., Tan, S.-C., Ren, J.-L., Liu, C.-G., ... Yao, X. (2012). Examination of causative link between a spring bloom and dry/wet deposition of Asian dust in the Yellow Sea, China. *Journal of Geophysical Research: Atmospheres*, *117*(D17). Retrieved 2023-07-27, from https://onlinelibrary.wiley.com/doi/abs/10.1029/2012JD017983 (_eprint: https://onlinelibrary.wiley.com/doi/pdf/10.1029/2012JD017983) doi: 10.1029/2012JD017983

Sosdian, S. M., Greenop, R., Hain, M. P., Foster, G. L., Pearson, P. N., & Lear, C. H. (2018, September). Constraining the evolution of Neogene ocean carbonate chemistry using the boron isotope pH proxy. *Earth and Planetary Science Letters*, *498*, 362–376. Retrieved 2021-09-01, from https://www.sciencedirect.com/science/article/pii/S0012821X1830356X doi: 10.1016/j.epsl.2018.06.017

Steinacher, M., Joos, F., Frölicher, T. L., Bopp, L., Cadule, P., Cocco, V., ... Segschneider, J. (2010, March). Projected 21st century decrease in marine productivity: a multi-model analysis. *Biogeosciences*, *7*(3), 979–1005. Retrieved 2023-08-08, from https://bg.copernicus.org/articles/7/979/2010/bg-7-979-2010.html (Publisher: Copernicus GmbH) doi: 10.5194/bg-7-979-2010

Steinthorsdottir, M., Coxall, H. K., de Boer, A. M., Huber, M., Barbolini, N., Bradshaw, C. D., ... Strömberg, C. A. E. (2021, April). The Miocene: The Future of the Past. *Paleoceanography and Paleoclimatology*, *36*(4). Retrieved 2021-05-06, from https://onlinelibrary.wiley.com/doi/10.1029/2020PA004037 doi: 10.1029/2020PA004037

Tagliabue, A., Bopp, L., & Aumont, O. (2008, January). Ocean biogeochemistry exhibits contrasting responses to a large scale reduction in dust deposition. *Biogeosciences*, *5*(1), 11–24. Retrieved 2023-06-28, from https://bg.copernicus.org/articles/5/11/2008/bg-5-11-2008.html (Publisher: Copernicus GmbH) doi: 10.5194/bg-5-11-2008

Tagliabue, A., Bopp, L., & Aumont, O. (2009). Evaluating the importance

of atmospheric and sedimentary iron sources to Southern Ocean biogeochemistry. *Geophysical Research Letters*, *36*(13). Retrieved 2023-06-28, from https://onlinelibrary.wiley.com/doi/abs/10.1029/2009GL038914 (_eprint: https://agupubs.onlinelibrary.wiley.com/doi/pdf/10.1029/2009GL038914) doi: 10.1029/2009GL038914

Tan, N., Zhang, Z. S., Guo, Z. T., Guo, C. C., Zhang, Z. J., He, Z. L., & Ramstein, G. (2022). Recognizing the Role of Tropical Seaways in Modulating the Pacific Circulation. *Geophysical Research Letters*, *49*(19), e2022GL099674. Retrieved 2023-08-18, from https://onlinelibrary.wiley.com/doi/abs/10.1029/2022GL099674 (_eprint: https://agupubs.onlinelibrary.wiley.com/doi/pdf/10.1029/2022GL099674) doi: 10.1029/2022GL099674

Tardif, D., Sarr, A.-C., Fluteau, F., Licht, A., Kaya, M., Ladant, J.-B., ... Banfield, W. (2023, August). The role of paleogeography in Asian monsoon evolution: a review and new insights from climate modelling. *Earth-Science Reviews*, *243*, 104464. Retrieved 2023-08-04, from https://linkinghub.elsevier.com/retrieve/pii/S0012825223001538 doi: 10.1016/j.earscirev.2023.104464

Tardif, D., Toumoulin, A., Fluteau, F., Donnadieu, Y., Le Hir, G., Barbolini, N., ... Dupont-Nivet, G. (2021, October). Orbital variations as a major driver of climate and biome distribution during the greenhouse to icehouse transition. *Science Advances*, *7*(43), eabh2819. Retrieved 2023-09-06, from https://www.science.org/doi/10.1126/sciadv.abh2819 doi: 10.1126/sciadv.abh2819

Tauxe, L., & Feakins, S. J. (2020). A Reassessment of the Chronostratigraphy of Late Miocene C3–C4 Transitions. *Paleoceanography and Paleoclimatology*, *35*(7), e2020PA003857. Retrieved 2022-07-19, from http://onlinelibrary.wiley.com/doi/abs/10.1029/2020PA003857 (_eprint: https://agupubs.onlinelibrary.wiley.com/doi/pdf/10.1029/2020PA003857) doi: 10.1029/2020PA003857

Valcke, S. (2013, March). The OASIS3 coupler: a European climate modelling community software. *Geoscientific Model Development*, *6*(2), 373–388. Retrieved 2022-01-03, from https://gmd.copernicus.org/articles/6/373/2013/ doi: 10.5194/gmd-6-373-2013

Wang, C., Dai, J., Zhao, X., Li, Y., Graham, S. A., He, D., ... Meng, J. (2014, May). Outward-growth of the Tibetan Plateau during the Cenozoic: A review. *Tectonophysics*, *621*, 1–43. Retrieved 2022-07-06, from https://linkinghub.elsevier.com/retrieve/pii/S0040195114000729 doi: 10.1016/j.tecto.2014.01.036

Wright, J. D., & Miller, K. G. (1996). Control of North Atlantic Deep Water Circulation by the Greenland-Scotland Ridge. *Paleoceanography*, *11*(2), 157–170. Retrieved 2022-07-06, from http://onlinelibrary.wiley.com/doi/abs/10.1029/95PA03696 (_eprint: https://agupubs.onlinelibrary.wiley.com/doi/pdf/10.1029/95PA03696) doi: 10.1029/95PA03696

Yang, R., Yang, Y., Fang, X., Ruan, X., Galy, A., Ye, C., ... Han, W. (2019). Late Miocene Intensified Tectonic Uplift and Climatic Aridification on the Northeastern Tibetan Plateau: Evidence From Clay Mineralogical and Geochemical Records in the Xining Basin. *Geochemistry, Geophysics, Geosystems*, *20*(2), 829–851. Retrieved 2022-07-20, from http://onlinelibrary.wiley.com/doi/abs/10.1029/2018GC007917 (_eprint: https://agupubs.onlinelibrary.wiley.com/doi/pdf/10.1029/2018GC007917) doi: 10.1029/2018GC007917

Zhang, L., Chen, M., Xiang, R., Zhang, L., & Lu, J. (2009, June). Productivity and continental denudation history from the South China Sea since the late Miocene. *Marine Micropaleontology*, *72*(1-2), 76–85. Retrieved 2020-11-09, from https://linkinghub.elsevier.com/retrieve/pii/S0377839809000383 doi: 10.1016/j.marmicro.2009.03.006

Zhang, Z., Ramstein, G., Schuster, M., Li, C., Contoux, C., & Yan, Q. (2014, September). Aridification of the Sahara desert caused by Tethys Sea shrinkage during the Late Miocene. *Nature*, *513*(7518), 401–404. Retrieved 2022-09-22, from http://

1176 www.nature.com/articles/nature13705 doi: 10.1038/nature13705

Figure_1.

A

Mio300Dust - Mio560Dust

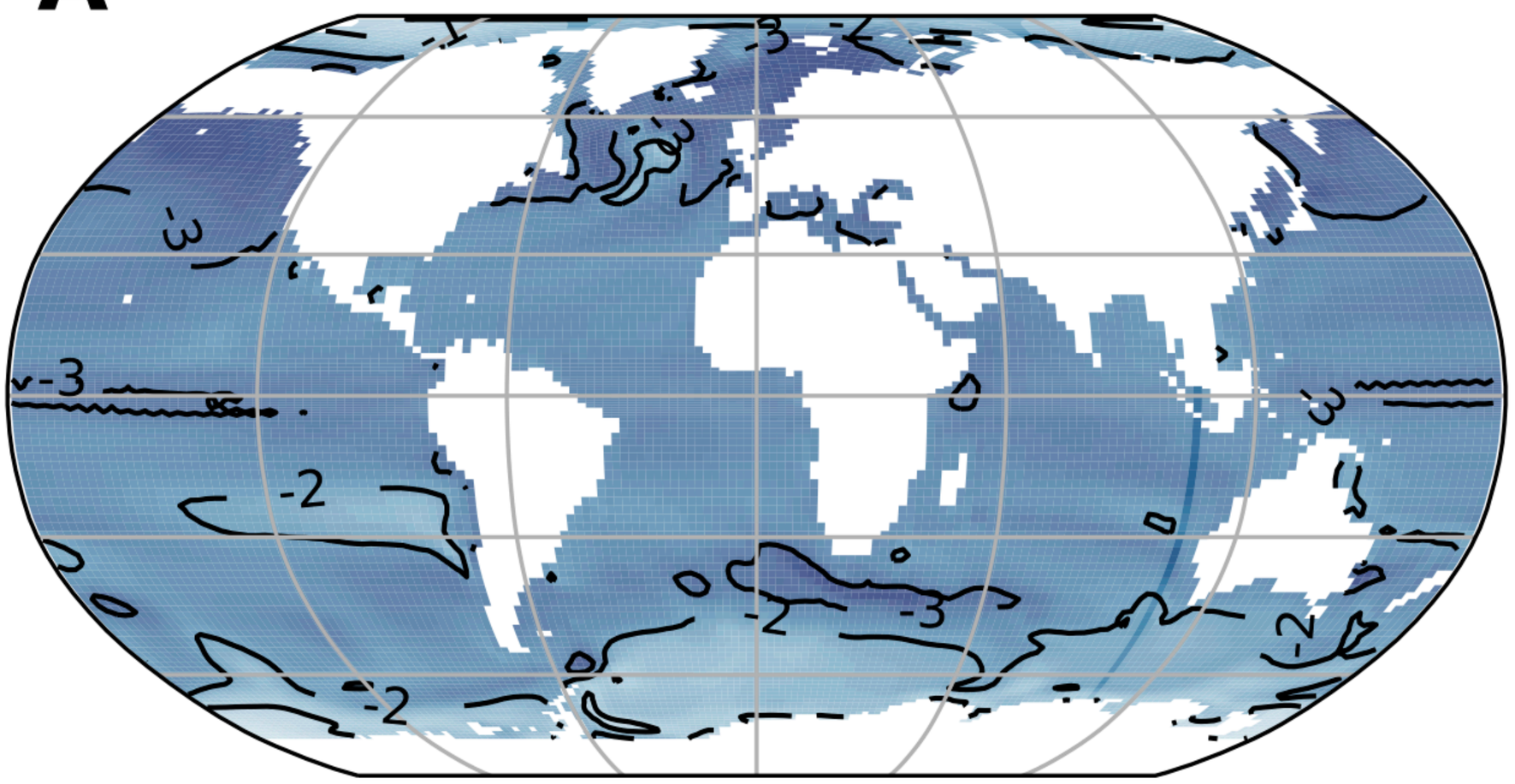

B

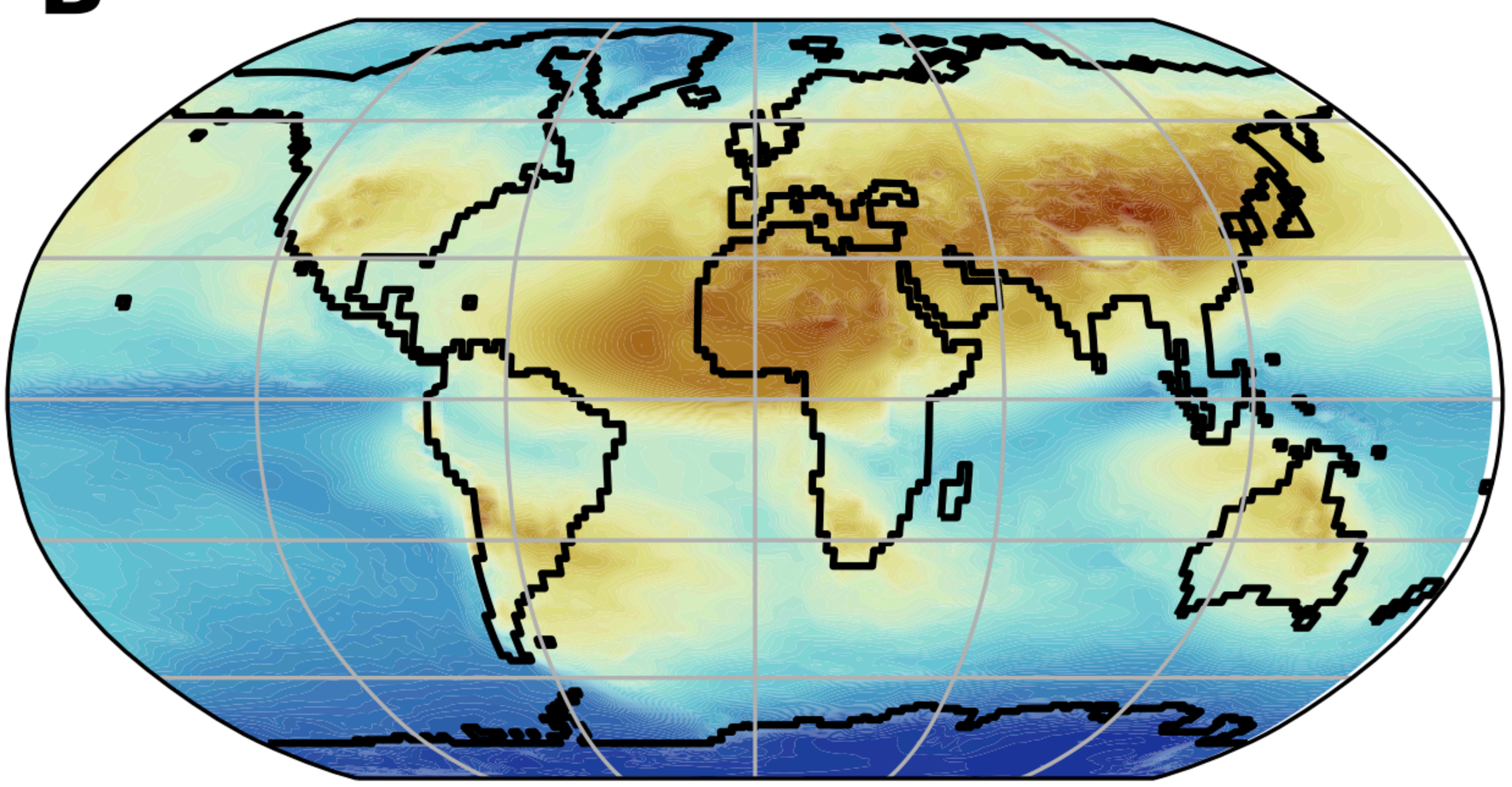

C

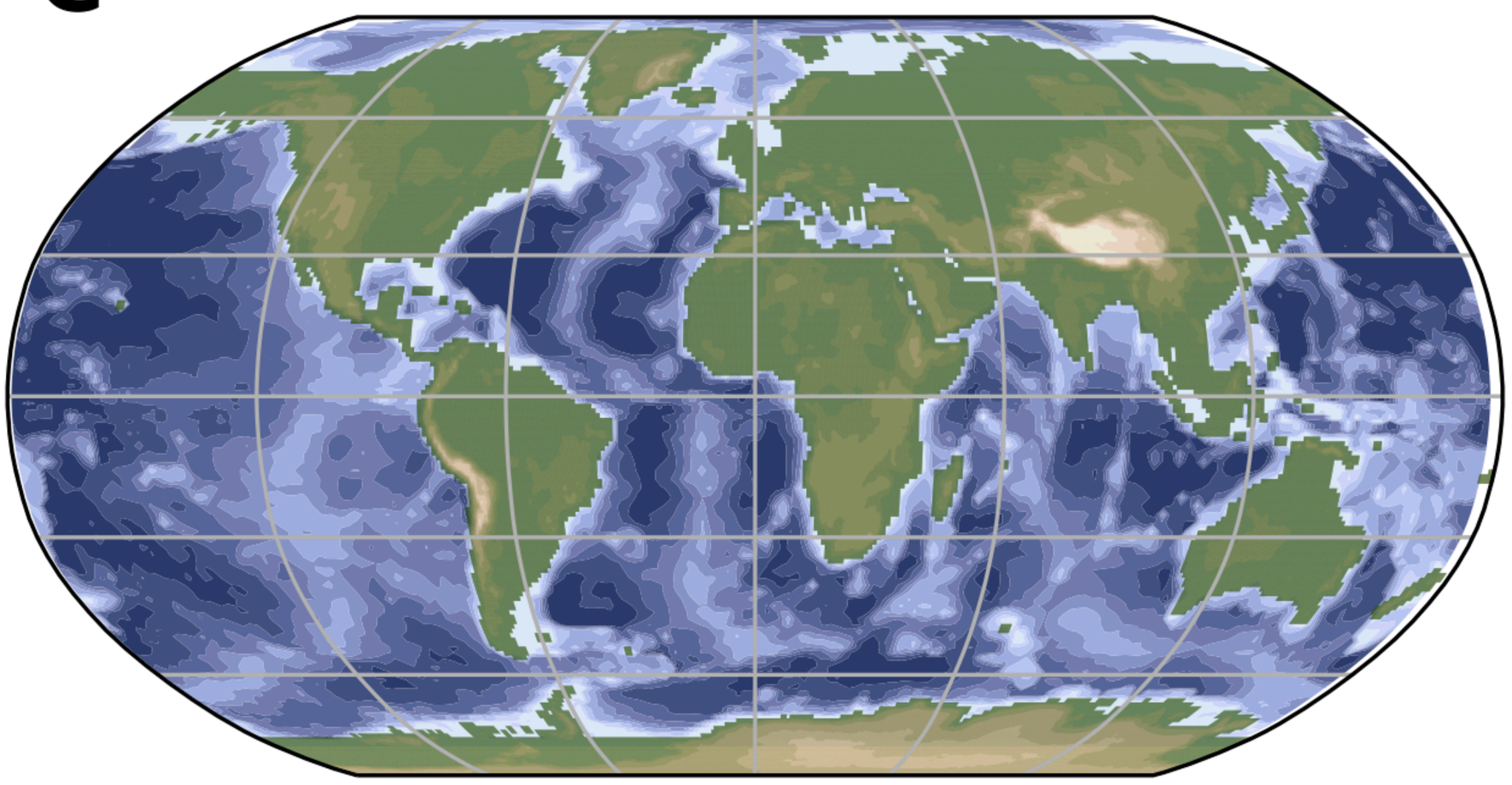

Figure_2.

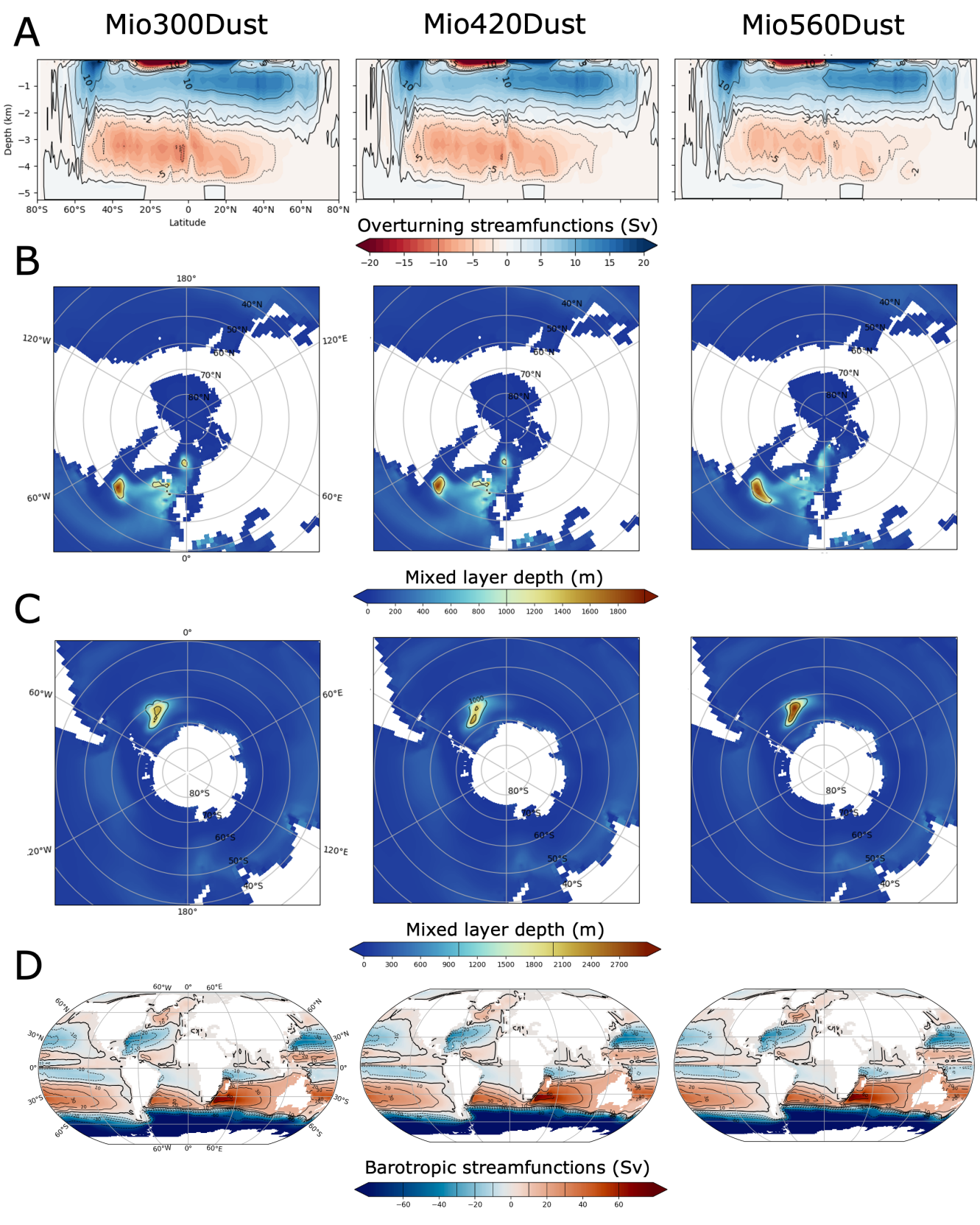
A
Mio300Dust
Mio420Dust
Mio560Dust
Depth (km)
Latitude
Overturning streamfunctions (Sv)
B
Mixed layer depth (m)
C
Mixed layer depth (m)
D
Barotropic streamfunctions (Sv)

Figure_3.

A

Mio420Dust

P1

P2

B

Mio300Dust

P3

0.0 0.1 0.2 0.3 0.4 0.5 0.6 0.7 0.8 0.9

Productivity by phyto (g/m^2/day)

C

Mio420Dust - Mio420NoDust

D

Mio300Dust - Mio560Dust

−0.20 −0.15 −0.10 −0.05 0.00 0.05 0.10 0.15 0.20

Δ Productivity by phyto (g/m^2/day)

Figure_4.

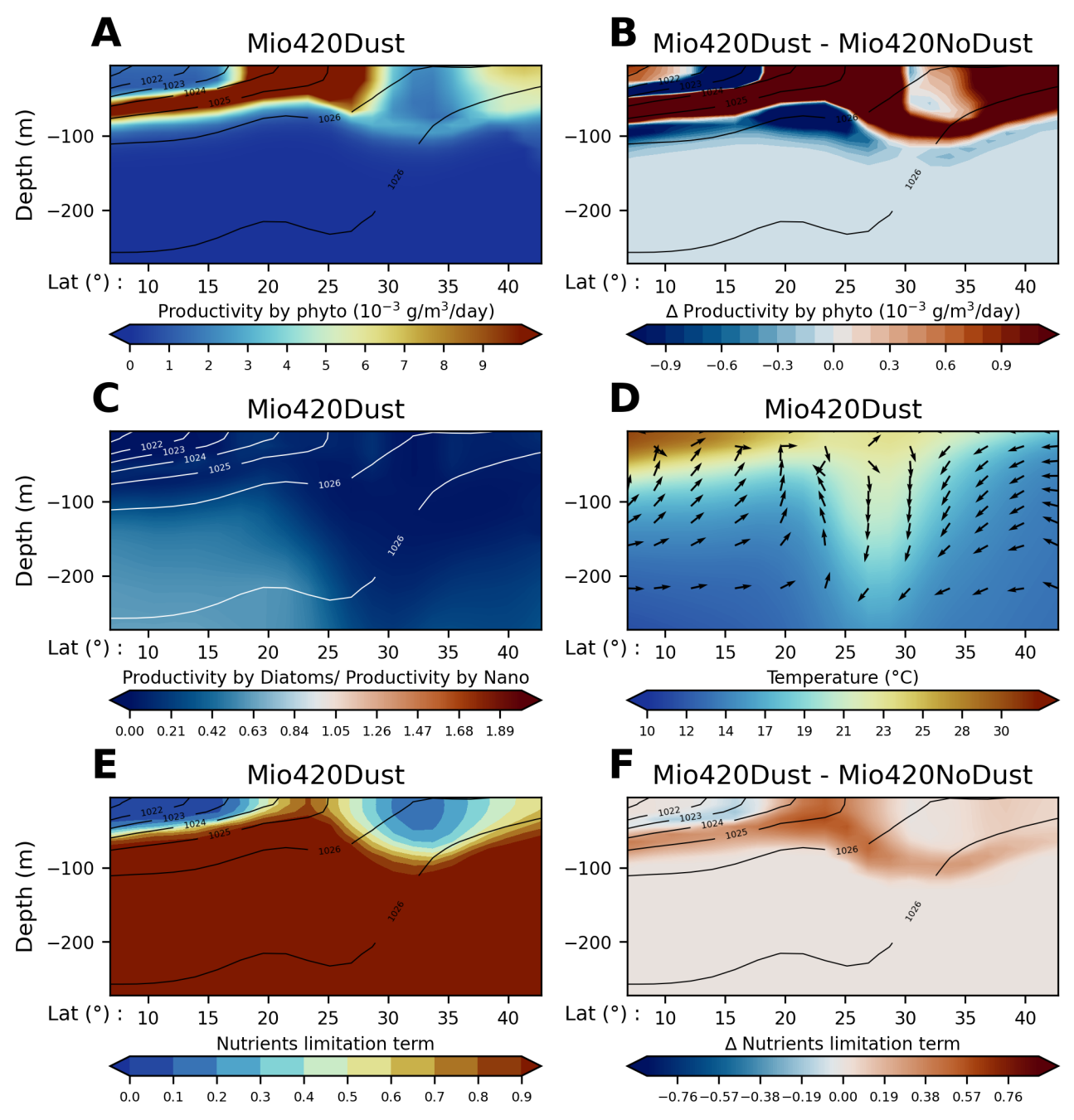
A
Mio420Dust
B
Mio420Dust - Mio420NoDust
C
Mio420Dust
D
Mio420Dust
E
Mio420Dust
F
Mio420Dust - Mio420NoDust
Depth (m)
−100
−200
Lat (°) :
10
15
20
25
30
35
40
1022
1023
1024
1025
1026
Productivity by phyto (10^{-3} g/m^3/day)
0 1 2 3 4 5 6 7 8 9
Δ Productivity by phyto (10^{-3} g/m^3/day)
−0.9 −0.6 −0.3 0.0 0.3 0.6 0.9
Productivity by Diatoms/ Productivity by Nano
0.00 0.21 0.42 0.63 0.84 1.05 1.26 1.47 1.68 1.89
Temperature (°C)
10 12 14 17 19 21 23 25 28 30
Nutrients limitation term
0.0 0.1 0.2 0.3 0.4 0.5 0.6 0.7 0.8 0.9
Δ Nutrients limitation term
−0.76 −0.57 −0.38 −0.19 0.00 0.19 0.38 0.57 0.76

Figure_5.

A

B

C

Productivity by phyto (g/m^2/day)

0.007
0.006
0.005
0.004
0.003

Mio420Dust
Mio420Dust2
Mio420Dust10
Mio420NoDust

Nutrient limitation term

1.0
0.9
0.8
0.7
0.6

Less limited productivity

More limited productivity

Dust deposition (mmol/m^2/day)

0.06
0.04
0.02
0.00

Jan Feb Mar Apr May Jun Jul Aug Sep Oct Nov Dec

Figure_6.

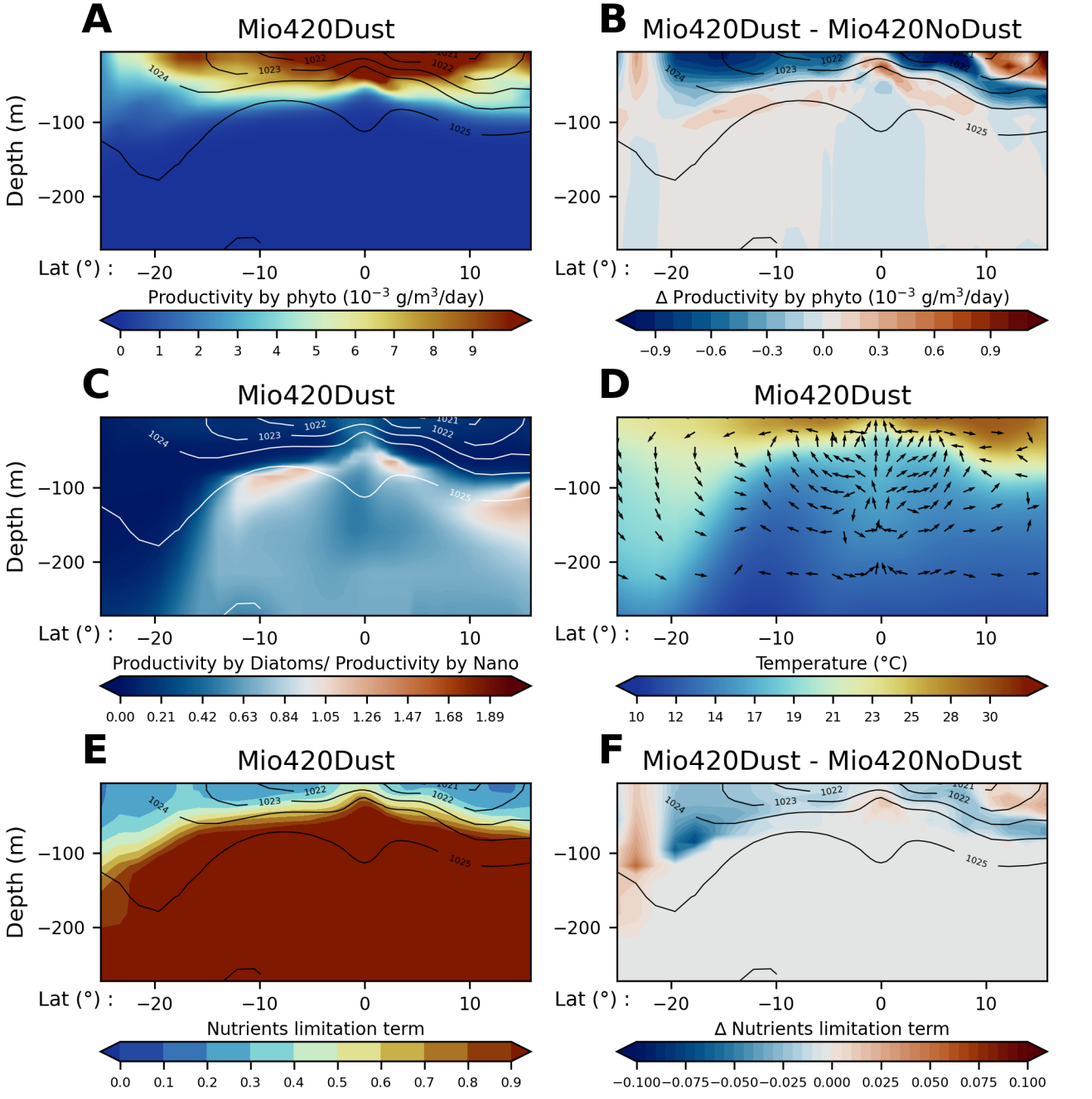
A
Mio420Dust
B
Mio420Dust - Mio420NoDust
C
Mio420Dust
D
Mio420Dust
E
Mio420Dust
F
Mio420Dust - Mio420NoDust
Depth (m)
−100
−200
Lat (°) :
−20
−10
0
10
1021
1022
1023
1024
1025
Productivity by phyto (10^{-3} g/m^3/day)
0 1 2 3 4 5 6 7 8 9
Δ Productivity by phyto (10^{-3} g/m^3/day)
−0.9 −0.6 −0.3 0.0 0.3 0.6 0.9
Productivity by Diatoms/ Productivity by Nano
0.00 0.21 0.42 0.63 0.84 1.05 1.26 1.47 1.68 1.89
Temperature (°C)
10 12 14 17 19 21 23 25 28 30
Nutrients limitation term
0.0 0.1 0.2 0.3 0.4 0.5 0.6 0.7 0.8 0.9
Δ Nutrients limitation term
−0.100 −0.075 −0.050 −0.025 0.000 0.025 0.050 0.075 0.100

Figure_7.

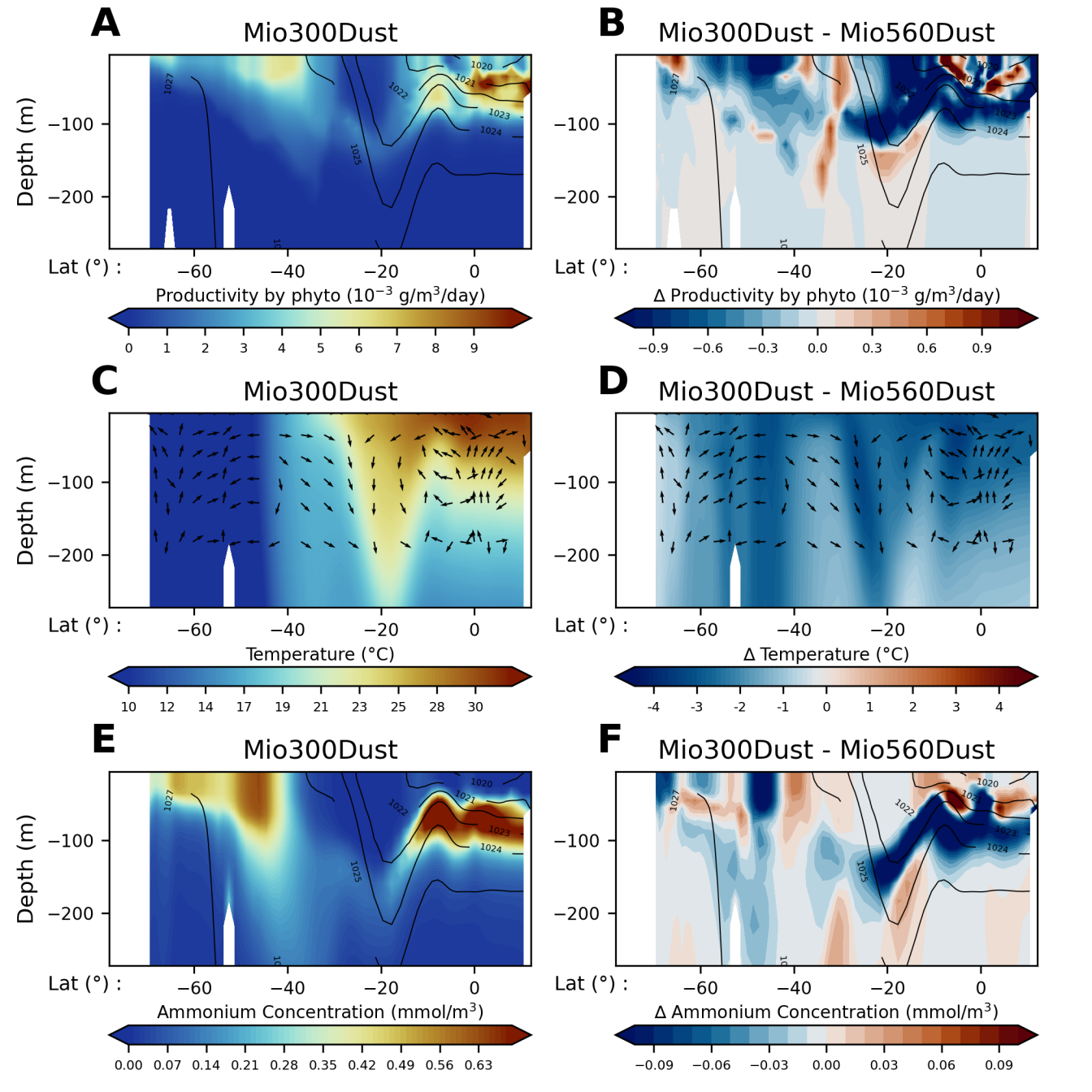
A
Mio300Dust
B
Mio300Dust - Mio560Dust
C
Mio300Dust
D
Mio300Dust - Mio560Dust
E
Mio300Dust
F
Mio300Dust - Mio560Dust
Depth (m)
−100
−200
Lat (°) :
−60
−40
−20
0
Productivity by phyto (10^{-3} g/m^3/day)
0 1 2 3 4 5 6 7 8 9
Δ Productivity by phyto (10^{-3} g/m^3/day)
−0.9 −0.6 −0.3 0.0 0.3 0.6 0.9
Temperature (°C)
10 12 14 17 19 21 23 25 28 30
Δ Temperature (°C)
-4 -3 -2 -1 0 1 2 3 4
Ammonium Concentration (mmol/m^3)
0.00 0.07 0.14 0.21 0.28 0.35 0.42 0.49 0.56 0.63
Δ Ammonium Concentration (mmol/m^3)
−0.09 −0.06 −0.03 0.00 0.03 0.06 0.09

Figure_8.

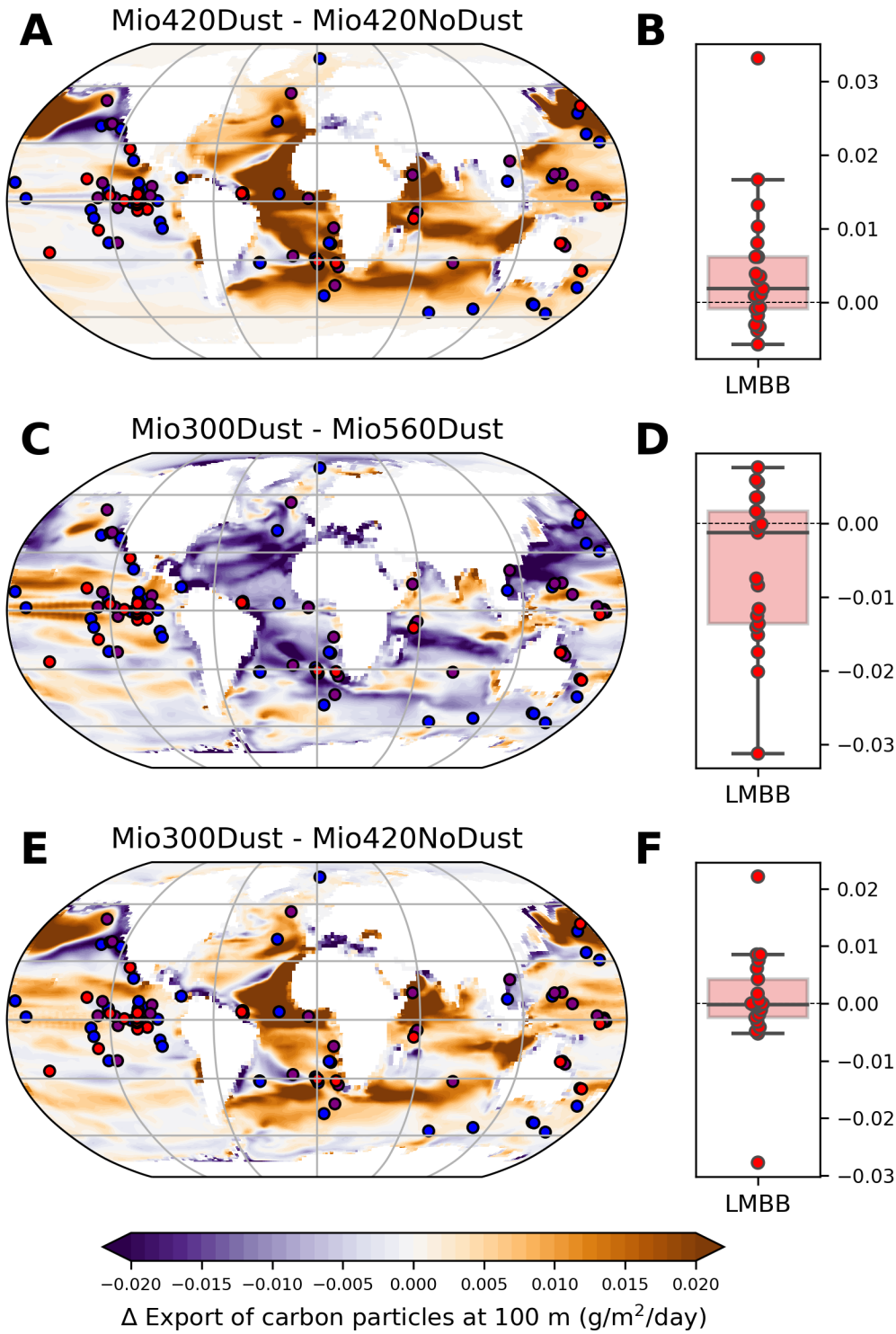
A
Mio420Dust - Mio420NoDust
B
0.03
0.02
0.01
0.00
LMBB
C
Mio300Dust - Mio560Dust
D
0.00
−0.01
−0.02
−0.03
LMBB
E
Mio300Dust - Mio420NoDust
F
0.02
0.01
0.00
−0.01
−0.02
−0.03
LMBB
−0.020 −0.015 −0.010 −0.005 0.000 0.005 0.010 0.015 0.020
Δ Export of carbon particles at 100 m (g/m^2/day)